Dalton Transactions

ROYAL SOCIETY OF CHEMISTRY

PAPER

View Article Online
View Journal | View Issue

Cite this: *Dalton Trans.*, 2025, **54**, 14286

Clicking [Mo(CO)$_3$(triphos)] to an azide-terminated alkylthiol SAM: structural, spectroscopic and electrochemical investigations†

Niels Michaelis, [a] Tobias A. Engesser, [a] Jan Krahmer,[a] Thomas Strunskus, [b] Christian Näther, [a] Nicolas Le Poul *[c] and Felix Tuczek *[a]

Received 23rd May 2025,
Accepted 18th July 2025

DOI: 10.1039/d5dt01217a

rsc.li/dalton

The synthesis and characterization of a new, linear triphos-type pincer ligand furnished with an ethynyl moiety in the ligand backbone (etPP^{PhTMS}P) and the derived tricarbonyl complex [Mo(CO)$_3$(etPP^{PhTMS}P)] are described. Deprotection of the latter leads to [Mo(CO)$_3$(etPP^{PhH}P)] which in turn is clicked onto an N_3-terminated Au-surface. The resulting monolayer is characterized by XPS, IRRAS and cyclic voltammetry, providing information on its chemical composition, the degree of surface coverage and the orientation of the headgroup. On the basis of these results, a protocol for the functionalization of surfaces with redox-active transition metal complexes for applications in, *e.g.*, electrocatalysis is developed.

Introduction

Transition metal based catalysts are involved in 90% of all chemical transformations.[1,2] Homogeneous catalysts based on defined molecular complexes can exhibit activities and selectivities exceeding those of most heterogeneous systems.[3,4] Nevertheless, difficult product separation and low stability often limit cost efficiency and scalability by industrial standards.[5] Immobilization of molecular catalysts onto solid supports has the potential to mitigate some of these drawbacks by creating more robust synthetic systems that essentially combine the strengths of homogenous and heterogeneous catalysis.[6,7] This approach may also be applied to the area of electrocatalysis by immobilizing electroactive transition-metal complexes on electrodes. Several promising results of this strategy have already been achieved in, *e.g.*, CO_2-reduction,[8] proton reduction[9] or ammonia oxidation.[10] In general, deposition onto an electrode surface may be furnished by non-covalent,[11] covalent[12,13] or polymerization-based binding of a transition-metal complex.[14] Each approach usually requires specific modifications in the ligand backbone of the targeted catalyst, ranging from implementation of extended aromatic frameworks (adhesion by π-stacking)[15] or introduction of specific bulky substituents (host–guest interactions)[10] to addition of reactive functional groups such as thiols,[16,17] phosphates, carboxylates,[18] or ethynyls.[19,20] These anchoring groups usually determine the types of feasible substrates and *vice versa*.

One research field to adapt this heterogenization approach is nitrogen fixation (nitrogen reduction reaction, N_2RR). As early as 1977 Pickett *et al.* functionalized SnO_2-electrodes with Chatt-type Mo(0)N_2-complexes with the goal to realize an electrocatalytic conversion of N_2 to ammonia (Scheme 1).[21] This pioneering work was followed by DuBois (1984)[22] and George *et al.* (1990)[23] who covalently attached Chatt-type molybdenum complexes to polymers. In the former case, the resulting polymer was deposited on an electrode.

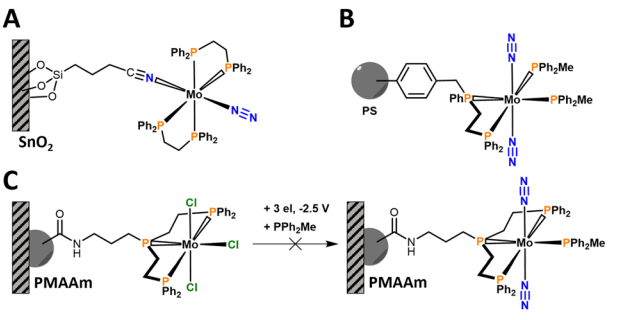

Scheme 1 Schematic depiction of immobilized N_2-complexes onto electrode surfaces or polymers making use of SnO_2- (A) or polystyrene-coated electrodes (B) or polymethacrylamide functionalized polymers (C).[21–23]

[a]*Institut für Anorganische Chemie, Christian-Albrechts-Universität zu Kiel, Max-Eyth-Straße 2, 24118 Kiel, Germany. E-mail: ftuczek@ac.uni-kiel.de*
[b]*Institute of Materials Science, Christian-Albrechts-Universität zu Kiel, Kaiserstraße 2, 24143 Kiel, Germany. E-mail: ts@tf.uni-kiel.de*
[c]*Laboratoire de Chimie, Électrochimie Moléculaires et Chimie Analytique (UMR CNRS 6521), Université de Bretagne Occidentale, 6 Avenue Le Gorgeu, 29238 Brest, France. E-mail: Lepoul@univ-brest.fr*

†Electronic supplementary information (ESI) available. CCDC 2452994, 2452996 and 2452995. For ESI and crystallographic data in CIF or other electronic format see DOI: https://doi.org/10.1039/d5dt01217a

Several decades past these seminal studies, a number of potent molecular catalysts for N_2RR in homogeneous solution exist.[24–28] Whereas mononuclear catalysts operating by successive protonation and reduction steps still play a role, dinuclear systems mediating N_2-splitting *via* metal halide precursors exhibit higher catalytic activities.[29,30] Pincer-type ligands such as PNP,[31,32] PCP,[33] PPP[34,35] in conjunction with a number of transition metals (besides Mo)[36,37] have been crucial with respect to these developments.[38,39] Nevertheless, electrochemical studies based on the classic Chatt system [M$(N_2)_2$(dppe)$_2$] (dppe = 1,2-bis(diphenylphosphine)ethane, M = Mo, W) and [$MoBr_3$(PNP)] (PNP = 2,6-bis(di-tertbutylphosphinomethane)pyridine) have provided the first examples of catalytic, electrochemical N_2RR producing 13 eq. (Mo) and 11.3 eq. (W)[40] and 11.7 eq. NH_3, respectively.[41] With the whole field slowly moving from chemo- to electrocatalytic approaches,[37,42] immobilization of these molecular catalysts onto (electrode) surfaces is gaining interest again.

In the past years, our group has followed several strategies to deposit low-valent transition-metal complexes capable of activating small molecules onto metallic surfaces by physisorption (Fig. 1, top).[11,43–46] In case of N_2RR mediated by transition-metal complexes, the activation of coordinated N_2 is essential for protonation and subsequent reaction.[47,48] In order to explore the impact of deposition on a metallic surface on this property, we resorted to carbonyl complexes due to their higher stability.[49,50] In fact, substantial influences on the activation of CO were, *e.g.*, observed for $Mo(CO)_3$ complexes supported by azacalixpyridine ligands (Fig. 1, top).[11,43,44] Alternatively, we prepared $Mo(CO_3)$ units supported by PN^3P-pincer[45]- and PPP-tripod[46] ligands which in turn were covalently linked to the TATA-platform (TATA = triazatriangulenium cation).[51] After deposition on Au(111) (Fig. 1, middle, right), IR reflection absorption spectroscopy (IRRAS) again revealed an influence of the metallic substrate on the electronic structure of the complex.[45,46]

Apart from the mentioned electronic factors, enhancing the stability of the surface monolayer is important in order to apply such systems as modified electrodes in electrocatalysis. Our primary goal was therefore to replace the physisorption by a chemisorption approach through covalent attachment of molybdenum dinitrogen or carbonyl complexes to metallic sur-

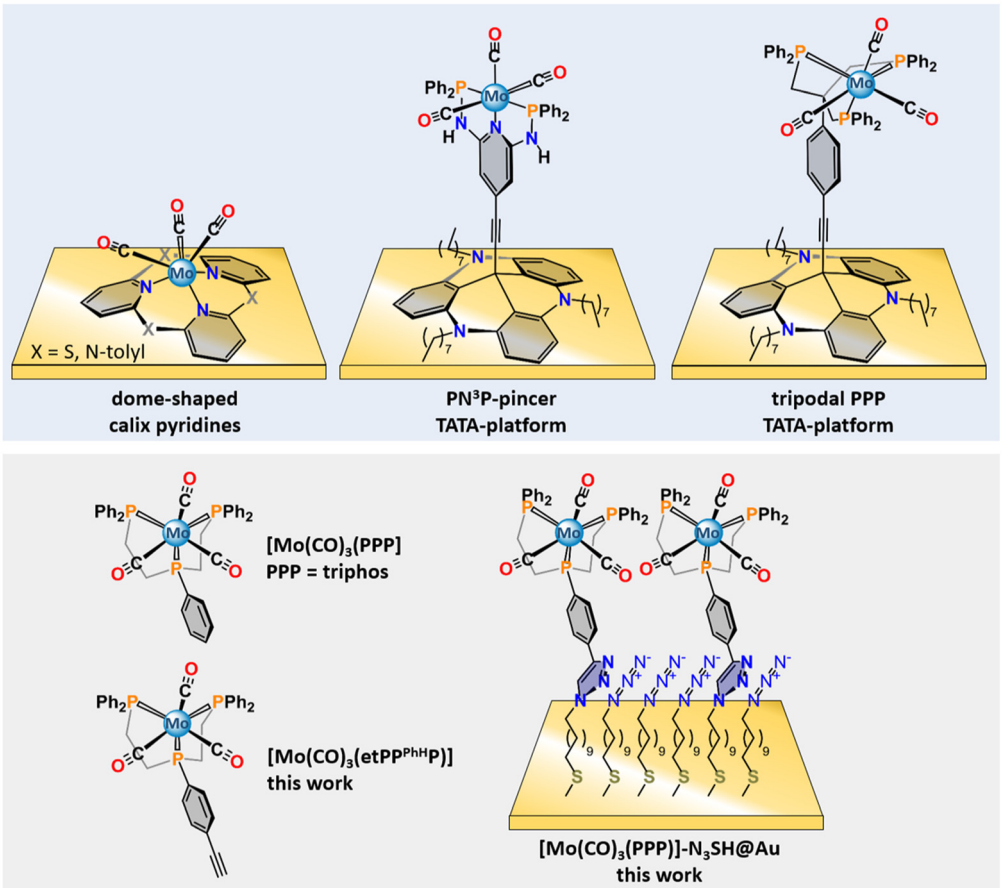

Fig. 1 Top: Physisorption *via* physical vapor deposition (pvd) or physisorption from solution as demonstrated with dome-shaped calixpyridine,[11] and TATA-based systems with pincer type PN^3P- or tripodal PPP-head groups (TATA = triazatriangulenium).[45,46] Bottom: Schematic depiction of the "classical" [$Mo(CO)_3$(PPP)] (PPP = triphos) reported by Chatt *et al.* and covalent attachment of this ethynyl functionalized motif *via* CuAAC as demonstrated in this work.

faces. In doing so, it is further essential to control the orientation and accessibility of the transition-metal headgroups. As demonstrated by polymer-immobilized $MoCl_3$-precursors, electrochemical reduction did not generate the corresponding MoN_2-complexes (Scheme 1C) due to poor accessibility of Mo-sites buried inside the surface-deposited polymer to N_2.[22]

On the background of the described results and concepts, we herein describe the functionalization of an Au(111) surface with a monolayer of a molybdenum tricarbonyl complex as a model system for an electrode functionalized with a Mo(0) dinitrogen complex that could be used for electrochemical N_2RR. By employing a linear tridentate, triphos-type[52] PPP ligand bearing an ethynyl-group at the central phenyl substituent we explore a stepwise surface functionalization protocol; *i.e.*, using this ethynyl function, the derived molybdenum tricarbonyl complex is grafted *via* copper(I)-catalysed azide–alkyne cycloaddition (CuAAC) onto an N_3-terminated Au(111) surface (Fig. 1, bottom right). The parent [$Mo(CO)_3$(triphos)] complex (Fig. 1, bottom left) has been extensively investigated during the last decades,[53–56] making this molecule a suitable platform to compare physicochemical properties in homogeneous solution with those of surface-grafted complexes. In this context, two aspects are of particular interest: (1) does the employed SAM-architecture reveal an influence of the metallic surface onto the observed CO-stretching modes? And (2) is the headgroup oriented in a way that potentially allows access of a gaseous substrate to the metal centers located at the surface/solution interface? Use of the $Mo(CO)_3$ unit as a spectroscopic probe will provide answers to both questions. In the following, the corresponding preparation protocols as well as the physicochemical properties of the resulting functionalized surface are described.

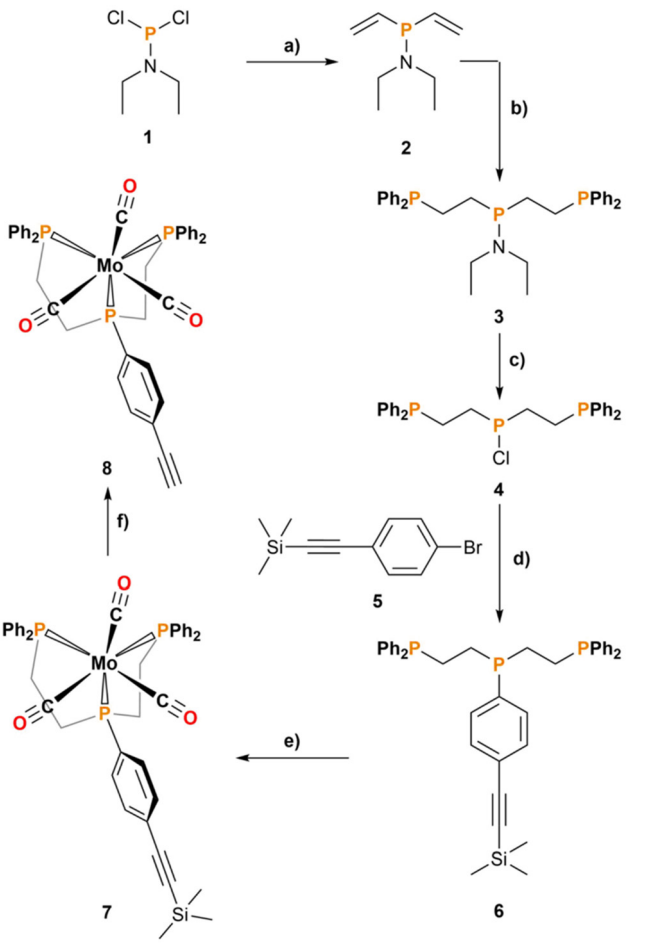

Scheme 2 Synthesis of [$Mo(CO)_3$(etPP^{PhTMS}P)] **7**, subsequent coordination and deprotection giving [$Mo(CO)_3$(etPP^{PhH}P)] **8**. (a) Vinylmagnesiumbromide (2 eq.), THF, −96 °C to rt, (b) $HPPh_2$ (2 eq.), KH, THF, 5 d, reflux, (c) eth. HCl (2.5 eq.), Et_2O, rt, (d) *n*-BuLi (1 eq.), THF, −96 °C to rt, (e) [$Mo(CO)_3$(cht)] (1 eq.) in abs. THF/*n*-pentane, 50 °C, (f) KOH (1.9 eq.), THF/MeOH (1 : 1), 50 °C.[49–51]

Results and discussion

Synthesis and characterization of [$Mo(CO)_3$(etPP^{PhH}P)] (8)

The ethynyl-functionalized PPP ligand was synthesized by adapting a synthetic route published by Miller *et al.* (Scheme 2).[57] Instead of using the *N*′*N*-diisopropylamine-protected precursors, we employed the corresponding diethylamine species. The divinyl compound $(vinyl)_2PNEt_2$ (**2**) was synthesized by adding a solution of vinylmagnesiumbromide to dichlorodiethylamino-phosphine (**1**), giving **2** as a pale colorless liquid in 70% yield. Terminal P-donors were introduced into the ligand backbone *via* KH-catalyzed hydrophosphination with $HPPh_2$ of both vinyl groups, leading to the formation of etPP^{NEt2}P (**3**) in quantitative yield (>95%) without need for further purification. Following deprotection *via* addition of etheric HCl to generate etPP^{Cl}P (**4**), the PPP moiety was reacted with 1-Bromo-4-trimethylsilyl-ethynylbenzene (**5**) adapting a published procedure.[58,59] To this end, **5** was lithiated with *n*-butyllithium by rapid lithium-halogen exchange, followed by dropwise addition of fresh **4**, thus forming etPP^{PhTMS}P (**6**) in 84% yield. The formation of the P–C bond to the phenylethynyl moiety was confirmed by ^{31}P NMR spectroscopy by the characteristic upfield shift of the central ^{31}P nucleus (t, $^3J(^{31}P,^{31}P)$) from 114.8 ppm in **4** (Fig. S7†) to −15.8 ppm in **6** (Fig. S10†). In contrast, no change in magnetic shielding occurs for the characteristic –PPh_2 signal (d, $^3J(^{31}P,^{31}P)$). This leads to an AB_2-type spin-system reminiscent of the classic "triphos" ligand.[60,61] The targeted carbonyl complexes were generated employing [$Mo(CO)_3$(cht)] (cht = cycloheptatriene) as a suitable precursor since the piano-stool-type orientation ensures selective *facial* coordination of ligand **6**. In a typical procedure a solution of [$Mo(CO)_3$(cht)] in *n*-pentane was added rapidly to a solution of **6** in THF at 50 °C in the dark to prevent photodissociation of the light- sensitive precursor. We observed better yields and higher purity of complex **7** at slightly elevated temperatures; presumably, faster ligand exchange kinetics prevent side reactions and photo-oxidation of the Mo^0-core during synthesis. Deprotection of the ethynyl moiety was achieved using 1.9 equivalents KOH in a mixture of THF and MeOH at 50 °C to give the target carbonyl complex

$[Mo(CO)_3(etPP^{PhH}P)]$ **8**. This route led to a product of higher purity compared to reverse processing (desilylation and subsequent complexation).

Crystallographic data

Crystals of $[Mo(CO)_3(etPP^{PhTMS}P)]$ (**7**) and $[Mo(CO)_3(etPP^{PhH}P)]$ (**8**) were obtained by slow evaporation of solutions in Et_2O (**7**) and THF (**8**) at rt in a glovebox and their structures were determined by SC-XRD. Both compounds crystallize in the triclinic crystal system in space group $P\bar{1}$ with two crystallographically independent complexes in the asymmetric unit (Fig. 2, Table 1 and Tables S19–S23†).

The Mo center forms a distorted MoC_3P_3 octahedron, with the Mo located slightly above the P1–P3–C2–C3 plane. Mo–P bond lengths range from 2.53 to 2.46 Å, with terminal Mo–P bonds (Mo–P2, Mo–P3 for **7** and Mo–P1, Mo–P3 for **8**) elongated compared to the central Mo–P bond, reflecting the differing σ-donating and π-backbonding properties of alkyl- *vs.* arylphosphines.[62] Alkylphosphines, as stronger σ-donors, form shorter Mo–P bonds. Despite this, the CO bond lengths (1.14–1.15 Å) remain unaffected in both **7** and **8**. Mo–C distances are 1.97–1.99 Å (**7**) and 1.98–1.99 Å (**8**). Structurally, **7** and **8** are similar but show distinct differences from the parent compound *fac*-$[Mo(CO)_3(PPP)]$.[55,56] The ethynyl group induces distortion in the $[Mo(CO)_3PPP]$ core, altering C–O and Mo–C distances in the equatorial plane. Mo–P bond lengths remain comparable across all three compounds, except for the central P–Mo-bond, which is slightly shorter in **7** and **8**, indicating an ethynyl influence. This is reflected in the tridentate bite angle (øA): 75.11° (**7**), 70.96° (**8**), *vs.* 72.0° for *fac*-$[Mo(CO)_3(PPP)]$.[55]

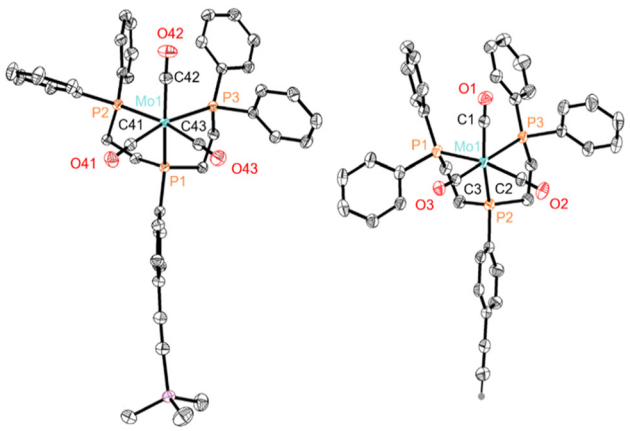

Fig. 2 Crystal structures of $[Mo(CO)_3(etPP^{PhTMS}P)]$ **7** (left) and $[Mo(CO)_3(etPP^{PhH}P)]$ **8** (right) shown as thermal ellipsoids with 70% probability. Please note that for both compounds only one of the two crystallographically independent complexes are shown. C is gray, P is orange, Mo is turquoise, O is red, Si is purple and all H atoms except for the C≡C–H moiety are omitted for clarity.

Table 1 Selected bond lengths [Å] and bite angle øA [°] crystallographic data for $[Mo(CO)_3(etPP^{PhTMS}P)]$ **7** and $[Mo(CO)_3(etPP^{PhH}P)]$ **8** compared to the classical $[Mo(CO)_3(PPP)]$.[55] Additional crystallographic information: see ESI†

fac-$[Mo(CO)_3L]$	L = triphos[55]	L = $etPP^{PhTMS}P$ (**7**)	L = $etPP^{PhH}P$ (**8**)
Mo–P	2.532(3)	2.5350(5) (*P2*)	2.5251(6) (*P1*)
Mo–P	2.479(2)	2.4630(5) (*P1*)	2.4686(6) (*P2*)
Mo–P	2.504(3)	2.5123(5) (*P3*)	2.4924(6) (*P3*)
Mo–C	1.99(1)	1.9994(19) (*C42*)	1.992(3) (*C1*)
Mo–C	1.96(1)	1.9731(19) (*C43*)	1.983(3) (*C2*)
Mo–C	1.96(1)	1.9834(19) (*C41*)	1.992(3) (*C3*)
C–O	1.16(1)	1.145(2) (*O42*)	1.151(3) (*O1*)
C–O	1.16(1)	1.159(2) (*O43*)	1.156(3) (*O2*)
C–O	1.15(1)	1.148(2) (*O41*)	1.144(3) (*O3*)
P_1–P_2–P_3 (øA)	72.0	75.11	70.96

NMR and IR spectroscopy

Successful formation of **7** and **8** was proven by ^{31}P and ^{13}C NMR spectroscopy, showing a large downfield shift for all three ^{31}P-nuclei compared to the free ligand (*cf.* Table S2 and Fig. S18, S23†) and $^2J(^{31}P, ^{31}P)$ coupling constants $^{obs}J_{P-P}$ = 3.0 Hz (**7**) and $^{obs}J_{P-P}$ = 3.1 Hz (**8**) of the *cis*-standing phosphine donors across the molybdenum center. The CO resonances of the $Mo(CO)_3$ fragment are split into two separate ^{13}C NMR signals at 226.5 and 222.17 ppm, corresponding to coordination of ^{13}CO in *axial* and *equatorial* position, respectively (Fig. S28†). While extraction of coupling constants is straightforward for the *dt*-pattern, the 8-line multiplet has to be simulated as part of an ABB'X-spin system. Overall, the coupling constants for **7** and **8** are very similar, which is expected, as the change from trimethylsilylethynyl- to ethynyl-substitution is distant from the molybdenum center and only slightly affects the electronic situation of metal and ligands (Table S2†).

Detailed evaluation of bulk IR data for complexes **7** and **8** is crucial for the correct interpretation of the IRRAS data, which is later used as surface characterization method after deposition of **8**. As a measure for the degree of small molecule activation the CO stretching bands of the $Mo(CO)_3$ unit can be used. Due to a strong Christiansen-effect,[63–65] samples had to be measured as suspensions in KBr, leading to an $A'_{(1)}$ CO stretching vibration at 1933 cm^{-1} for **7** and **8** (Fig. 3 and S29, S30†). Furthermore, the A'' and $A'_{(2)}$ modes exhibit bands at 1849 and 1826 cm^{-1} for **7** and a broad symmetrical band for **8**. Compared to the reported CO-stretches of *fac*-$[Mo(CO)_3(PPP)]$ with $A'_{(1)}$ = 1937 cm^{-1}, 1848 cm^{-1} for A'' and $A'_{(2)}$,[56] one can see that **7** and **8** have almost the same electronic structure as their parent complex. Changes in stretching frequencies after surface deposition can serve as a measure for changes in CO-activation on surface, which is investigated by IRRAS (see below).

Electrochemistry

To compare its electrochemical behavior with the parent complex *fac*-$[Mo(CO)_3(PPP)]$, compound **8** was analyzed by cyclic voltammetry (CV) in THF and DCM using Au, glassy carbon (GC), and Pt working electrodes with 100 mM NBu_4PF_6 supporting electrolyte under N_2. In THF, scanning from −0.25 V *vs.* Fc/Fc^+ towards positive potentials revealed an irreversible oxidation at E_{pa} = 0.15 V followed by a small cathodic peak at E_{pc} = −1.3 V on the reverse scan (Fig. 4A, black, peak (1)). This

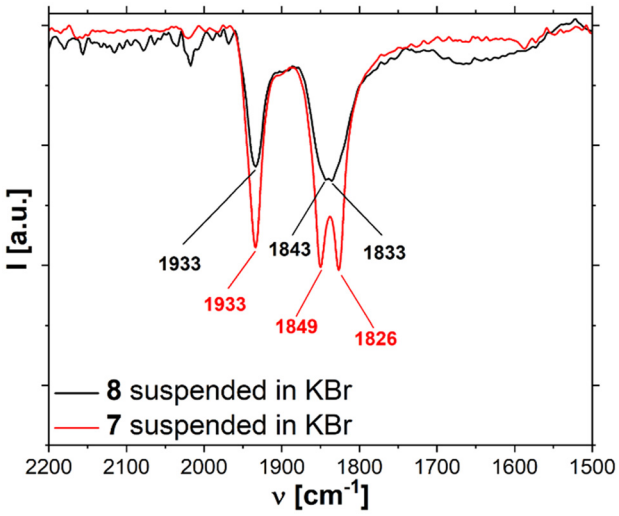

Fig. 3 CO stretching region of the IR spectra of **7** and **8** suspended in KBr.

reduction peak was not detected when sweeping initially towards negative potential values (Fig. 4A, red). Its peak current however significantly increased when holding the potential at 0.2 V for 30 s (Fig. 4A, grey). All these results corroborate the occurrence of a chemical reaction following the oxidation process at 0.15 V, leading to the generation a new species that is reduced at −1.30 V. The oxidation peak at 0.15 V remained irreversible whatever the scan rate ($0.02\ V\ s^{-1} < \nu < 2.0\ V\ s^{-1}$) in both solvents. Linear variation of peak currents with $\nu^{1/2}$ for these two processes confirmed that the electrode reaction is under diffusion control and not related to adsorbed species (Fig. S34–S39†). Diffusion coefficients were determined *via* ^{1}H-DOSY-NMR: $2.017 \times 10^{-9}\ m^2\ s^{-1}$ (THF-d^8) and $2.388 \times 10^{-9}\ m^2\ s^{-1}$ (DCM-d^2) (Fig. S42 and S43†). From these values, the number of electrons was determined for the oxidation process at 0.15 V (see ESI†). The calculations suggest that the oxidation process consistently involves a two-electron transfer across all electrodes, in agreement with reported data on *fac*-[Mo(CO)$_3$(PPP)] in DCM,[54] acetonitrile, and DMF[53] at 0.1 V *vs.* Fc/Fc$^+$. Interestingly, a secondary irreversible process was observed at potential values near −0.20 V in both solvents (Fig. 4A–C, peak (2)) and is ascribed to the *mer*-**8** isomer. Such

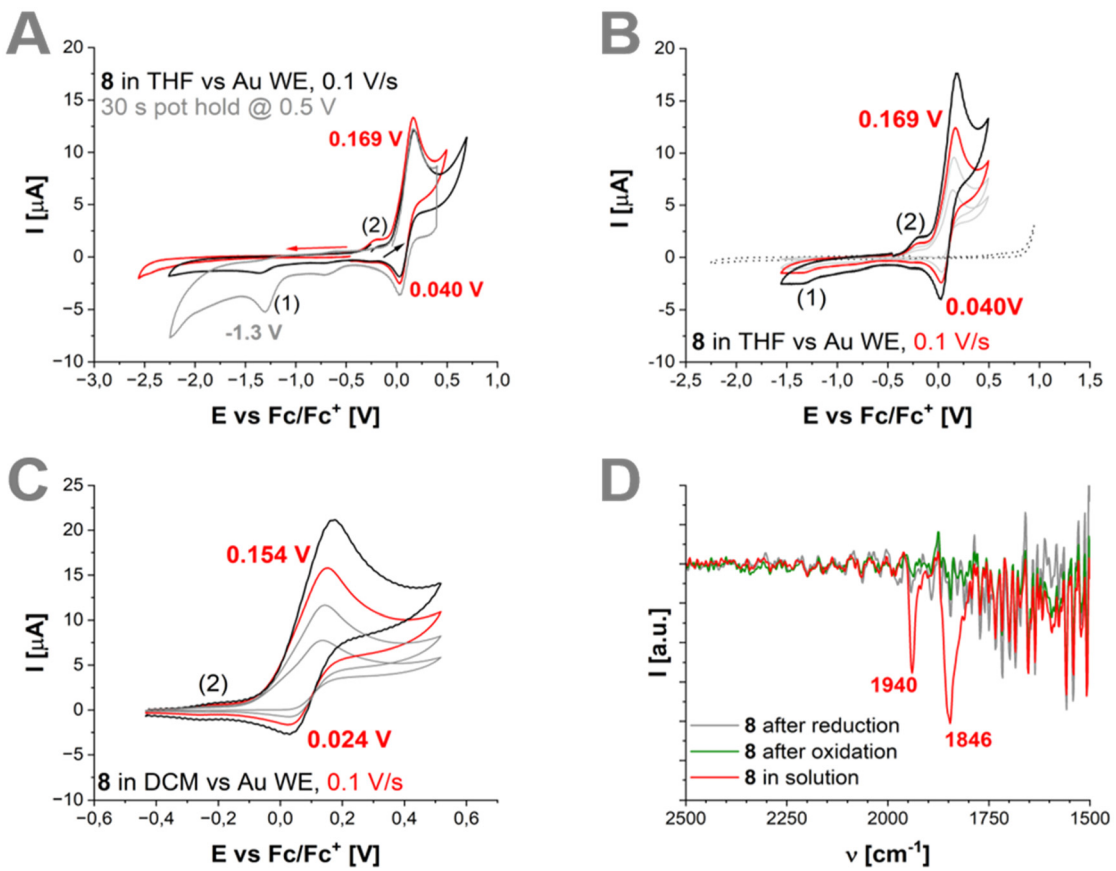

Fig. 4 CVs of 1 mM **8** in 100 mM NBu_4PF_6/THF or DCM under inert Atm. (A) Oxidation and reduction of **8** inside the potential limits of THF (Fig. S37†). Holding the oxidative potential increases i_{pc} at −1.3 V. (B) Oxidation of **8** in THF between $0.02\ V\ s^{-1} \leq \nu \leq 0.2\ V\ s^{-1}$ with electrochemical response of *mer*-**8** (2). (C) Oxidation of **8** in DCM between $0.02\ V\ s^{-1} \leq \nu \leq 0.2\ V\ s^{-1}$ with electrochemical response of *mer*-**8** (2). (D) IR-SEC of 20 mM **8** in 100 mM NBu_4PF_6 in THF before and during oxidation at 0.2 V vs Fc/Fc+ (red, green) and after back reduction to −1.3 V (grey).

fac^{+}/fac^{0} ⇌ mer^{+}/mer^{0} and fac^{0} ⇌ mer^{0} isomerization lability[53,54] in *fac*-[Mo(CO)$_3$(PPP)] was shown to be linked to irradiation into a ligand field transition (~330 nm). Herein, UV/vis data (Fig. S41†) suggests a similar transition (350–400 nm) for **8**, correlating the secondary system (2) at −0.1 V to *mer*-**8** as anticipated (Fig. 4A and B (2)). Traces of *mer*-**8** were absent in solution (Fig. S23†) but formed under illumination, likely *via* photoisomerization, as formation was suppressed in the dark (Fig. S37–S39†).

IR spectroelectrochemistry (IR-SEC) under Ar in THF (Fig. 4D) revealed intense CO stretches at 1940 ($A'_{(1)}$) and 1846 cm^{-1} ($A''/A'_{(2)}$) of *fac*-**8** (red curve). Upon oxidation, the IR signals disappeared, suggesting CO ligand dissociation (Fig. 4D, green curve). Even after immediate back-reduction, *fac*-**8** was not regenerated. These results suggest dissociation of all three CO ligands during two-electron oxidation (grey curve), consistent with earlier studies on [Mo(CO)$_3$(PPP)].[54] The resulting Mo(II) species generated upon oxidation is likely reduced at −1.3 V *vs.* Fc/Fc^{+} in both solvents (Fig. 4A and S35, S37†), with a potential comparable to the reduction of [MoCl$_3$(triphos)] (−1.50 V *vs.* Fc/Fc^{+}).[66]

Overall, crystallographic, vibrational, NMR, and electrochemical data show close agreement between [Mo(CO)$_3$(PPP)] and [Mo(CO)$_3$(etPP^{PhH}P)] (**8**). This allows differentiating surface influences from intrinsic molecular properties when binding **8** to a metallic substrate.

Surface studies

SAMs can be prepared and formed by employing thiols as anchor groups.[16,67] In the case of simple alkanethiols, the crystallinity, structure and therefore overall quality of the SAM is related to absorption time and chain length. To have reasonably ordered layers – while keeping the number of carbon atoms on the surface as low as possible – one has to carefully choose the number n of CH$_2$ groups included in the backbone. SAMs with n > 16 are considered to form pure crystalline phases whereas those with n < 9 can lead to disordered monolayers.[16,68–70] Therefore, we opted for 1-azide-11-undecanethiol as our building block, as with a chain length of eleven CH$_2$-groups (n = 11), the formed SAM should be crystalline enough to extract meaningful information from IRRAS-measurements while keeping the distance between Au-surface and metal center as small as possible. It is of interest to evaluate whether, by choosing this surface architecture, an influence of the underlying substrate onto the grafted metal complex and its spectroscopic properties is measurable.

Preparation of a N$_3$-terminated SAM on Au(111)

Preparation of functionalized Au-SAMs was achieved according to established procedures[71] by immersion of clean Au-substrates in 5 mM solutions of 1-azide-11-undecanethiol (**N$_3$SH**) in absolute EtOH over a duration of 48 h to ensure formation of the standing-up phase (Scheme 3a).[16,67] The pure N$_3$-terminated SAM on Au(111) (**N$_3$SH**@Au(111)) was subjected to XPS measurements to assess the overall quality of the monolayer (Fig. 5). Based on these experiments, differences between pre- and post-functionalization are easy to identify. The C 1s peak is well fitted with three species in the ratio of 82, 9 and 9% corresponding to the percentage of C–C, C–N and C–S bonds in **N$_3$SH** (Table S9†). The three peaks needed to fit the N 1s region are in good agreement with electronic structure of organic azides (RN$_3$).[72,73] The signal with a binding energy (BE) of 398.5 eV corresponds to minor irradiation damage.[74,75] The S 2p region indicates the presence of three different S-species, with the S 2p (3/2) peak of the main component at 162.0 eV corresponding to chemisorbed sulfur (Au–S).[16,76–78] The S 2p (3/2) peak at 163.3 eV reveals the presence of a significant amount of either free thiol or disulfide.[79,80] While free thiol is usually present due to inadequate washing[16] – which has been accounted for with the employed preparation protocol (see Experimental section) – the latter species is either associated to form on the Au-surface after chemisorption of

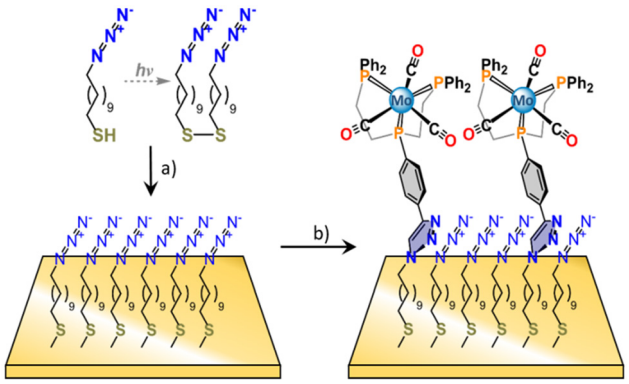

Scheme 3 Two step surface functionalization of Au(111) with **8**. Preparation of N$_3$-terminated Au(111) surface with 5 mM N$_3$SH (abs. EtOH) for 48 h (a). Covalent attachment of **8** *via* CuAAC for 2 h, rt, inert-atm (b).

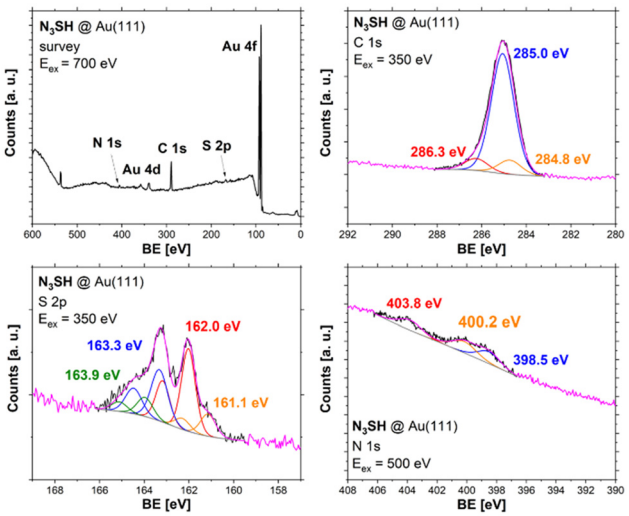

Fig. 5 XP spectra of an Au(111)–surface functionalized with a **N$_3$SH**-SAM. Survey (top left), C 1s- (top right), S 2p- (bottom left) and N 1s-region (bottom left). For fitting parameters see Table S9.†

free thiol[81] or corresponds to physisorbed chains stuck inside the SAM as observed in other studies.[79,82] Another small S 2p (3/2) peak at lower binding energies (161.1 eV) is clearly visible and is known to be atomic sulfur[16,83] or another form of bound thiolate.[84,85] A similar feature had to be fitted at higher binding energies (163.9 eV). These species usually correlate with a degradation of the SAM,[16,86] which can be caused by soft X-ray-[87] or UV irradiation.[88,89] Notably, SAMs are known to be quite unstable once formed, even when stored under inert conditions.[89–91]

To estimate the surface coverage of **N_3SH**@Au(111), we subjected **N_3SH**-functionalized Au-electrodes to reductive desorption experiments in 0.1 M NaOH.[92,93] Based on these results we calculate the surface concentration of the adlayer, Γ_m, between 5.96×10^{-10} and 9.20×10^{-10} mol cm^{-2} which ranges from slightly below to slightly above the theoretical value of $\Gamma_m = 8.0 \times 10^{-10}$ mol cm^{-2} (Fig. S46–S48†).[94] Similar values have been obtained experimentally under comparable conditions.[92,95] However, we noted a decrease of Γ_m depending upon whether freshly prepared **N_3SH** was used or not. We attribute this to the increasing amount of disulfide, which formed very quickly under our storage conditions (Fig. S31 and S33†) and likely leads to a SAM of lesser quality.[73,96]

Additionally, we examined the passivation of **N_3SH**@Au (111) in aqueous (0.1 M K_2SO_4, Ag/AgCl-ref) and organic (0.1 M NBu_4F_6, THF, Fc/Fc$^+$-ref) media against an external redox probe. High-quality alkylthiol SAMs can act as insulating layers, blocking electron transfer above a certain chain length.[16,67,97,98] This effect is reproduced when immersing a pre-treated Au-electrode in a **C_{16}SH** solution (Fig. S49,† left). However, **N_3SH**@Au-WE under identical conditions shows currents of 10–15 μA with a peak-to-peak separation of 1.03 V, suggesting increased tunnelling probability due to high -N_3 coverage or defect sites, which can facilitate charge transfer.[16,99–101] Studies on molecular diodes based on alkylthiol-SAMs showed that defects caused by impurities or different thiol precursors increase current leaking significantly.[96] On the other hand, previous studies on a mixed alkyl-N_3-terminated SAM (9 : 1) on Au(111) resulted in complete passivation towards external redox probes.[102,103] Increasing the surface concentration of terminal azide groups thus appears to reduce the passivation of the SAM.

In organic media, the electrochemical behaviour changes as both modified electrodes conduct towards an external redox probe like ferrocene (Fig. S49,† right). Peak-to-peak separation for **C_{16}SH**@Au-WE (268 mV) is higher than for **N_3SH**@Au-WE (76 mV), with both showing ~1.0 μA currents. This indicates that ferrocene likely penetrates the SAM backbone, lowering the overpotential for electron transfer compared to aqueous media. It is known that some organic molecules can even become trapped in SAMs when immersed in organic solvents.[104] Reduction of both electrodes to negative −2.0 V reveals peaks at −1.63 V (**N_3SH**@Au-WE) and −1.89 V (**C_{16}SH**@Au-WE) with i_{pc} between −1.2 and −0.6 μA (Fig. S50†), attributed to adlayer cleavage *via* Au–S bond reduction. This aligns with aqueous desorption studies where reduction peaks shift cathodically for SAMs with increasing number of CH_2 groups.[105]

Attachment of [Mo(CO)$_3$(etPP^{PhH}P)] onto N_3SH@Au(111)

Azide-terminated Au-surfaces can be functionalized with transition-metal complexes *via* copper(I)-catalysed azide–alkyne cycloaddition (CuAAC) under various conditions.[110,111] Evaluating surface integrity throughout this process is crucial. In order to attach the Mo(CO)$_3$ unit present in [Mo(CO)$_3$(etPP^{PhH}P)] (**8**) to the alkylthiol SAM **N_3SH**@Au(111) and optimize deposition conditions, we tested four copper catalysts and analysed the resulting **8-N_3SH**@Au(111) monolayer using XPS, IRRAS, and cyclic voltammetry (Table 2).

Preliminary tests with [CuBr(PPh$_3$)$_3$] ("**Click 2**", *cf.* Table 2) revealed unintended Cu–Mo interactions in solution (Fig. S44†), forming oxidized Mo^{VI} species on the surface (Fig. S45†), possibly due to ligand exchange reactions with CO. To minimize side reactions, we limited the reaction time to 2 h at room temperature (Scheme 3b). Still, **Click 2** failed to generate **8-N_3SH**@Au(111), as no Mo 3d peaks could be observed (Fig. S53†). Therefore, other Cu complexes were employed (*cf.* Table 2). In contrast to **Click 2**, catalysts **Click 1**, **3**, and **4** produced Mo(0) peaks at 228 and 231 eV with a 3 : 2 ratio and 3.1 eV spin–orbit splitting, confirming an intact Mo-moiety (Fig. S51–S55†).[43,45,46] However, the post-functionalization process also has a pronounced effect on the underlying Au–S interface with additional sulphur species forming during CuAAC (Fig. S51–S55†). Nevertheless, it is possible to functionalize the N_3-terminated surface with **Click 1**, **Click 3** and **Click 4** whereas **Click 2** was found to be ineffective in this regard.

IRRAS

Further investigation of **N_3SH**@Au(111) and **Click 1–4** was conducted by IRRAS to gather information on functionalization degree as well as on the orientation and structure of the generated monolayer (Fig. S57†). All functionalized surfaces exhibit strong absorptions in the range from 2200 to 1750 cm^{-1} due to the N_3 and CO stretching vibrations (Fig. 6). However, IRRA spectra of **Click 1**, **3** and **4** show intense CO absorptions together with the N_3 stretching vibration at 2102 cm^{-1} whereas, for **Click 2**, no CO stretches are visible, which corresponds to the obtained XPS data. Comparing **Click 1**, **3** and **4** indicates differences in $A'_{(1)}$, A'' and $A'_{(2)}$ intensities. This observation is due to the dependence of the IRRAS intensity of a given vibration on the orientation of the transition dipole

Table 2 Preparation of **8-N_3SH**@Au(111) with different Cu-catalysts. The exact preparation protocols are listed in the experimental section

	Cu-cat./additive (solvent)
Click 1	$CuSO_4 \cdot 5H_2O$/ascorbic acid (H_2O/EtOH)[106]
Click 2	[CuBr(PPh$_3$)$_3$]/NEt$_3$ (THF)[20,107]
Click 3	CuBr/NEt$_3$ (THF)[108]
Click 4	[Cu(MeCN)$_4$]PF$_6$/2,6-lutidine (THF)[109]

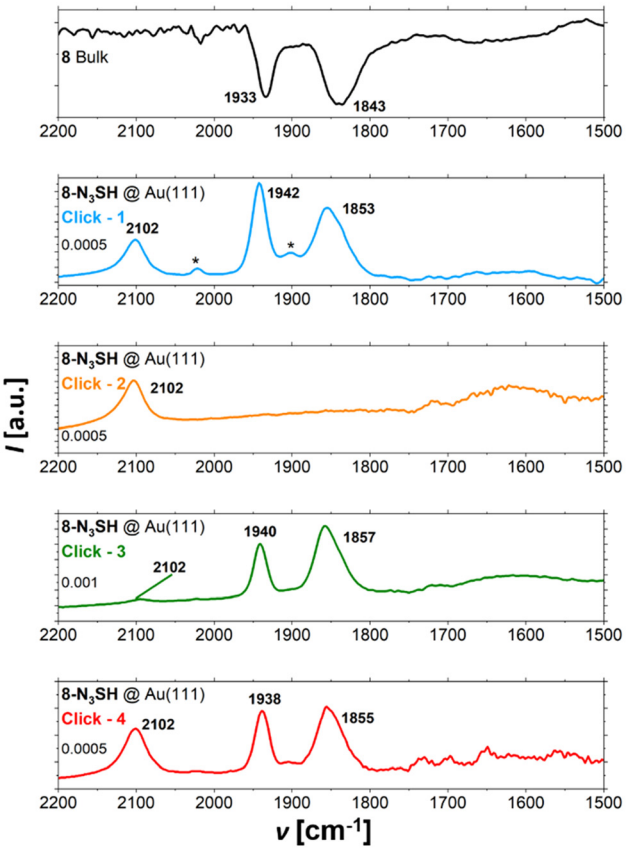

Fig. 6 Bulk IR of **8** and IRRA spectra of **8-N_3SH**@Au(111) prepared employing protocols **Click 1–4** in the CO-stretch region. The visible feature at 2102 cm^{-1} corresponds to unfunctionalized azides of the SAM backbone. * mark small portions of *mer*-**8**. For full spectrum see Fig. S57.†

moment relative to the surface.[112–114] Two methods are known in the literature for determining the orientation of functional groups deposited on surfaces from IRRAS intensities: the absolute method first reported by Allara and coworkers[115–117] and the RATIO method established by Debe *et al.*[118] Various reports based on the absolute[119–123] as well as the RATIO method exist.[113] Recently, Früh *et al.* published an updated approach to the interpretation of IRRAS data based on the latter technique.[114] To apply these equations to **8-N_3SH**@Au (111) we determined the intensity ratios $I_n^{SAM}/I_n^{(Bulk)} = R_n$ ($n = x$, y, z) whereby $R_x \rightarrow A'_{(2)}$, $R_y \rightarrow A''$ and $R_z \rightarrow A'_{(1)}$ (Fig. 7A and S62†). The intensity of, *e.g.*, the $A'_{(1)}$ vibration in the IRRAS spectrum is maximal if its transition dipole vector is oriented along the surface normal. In this case the intensities of both A'' and $A'_{(2)}$ stretches are zero. Any deviation from this configuration will give non-vanishing A'' and $A'_{(2)}$ intensities. Due to the high symmetry of **8**, the A''- and $A'_{(2)}$ -vibrations significantly overlap (Fig. 3). In order to extract reliable intensity values for all CO-vibrations, bulk IR- (Fig. S60†) and IRRA spectra (Fig. S58 and 59†) were deconvoluted, as demonstrated for **Click 1** (Fig. 7B). The intensity ratios R_n, R_{yx} and R_{xz} together with the calculated values of θ and Ψ are collected in Table 3. Notably, both θ and Ψ only vary in a range of approximately 5° when compared within the different protocols. Therefore, the nature of the employed catalyst has little effect on the resulting headgroup orientation.

As shown for **Click 1** in Fig. 7C and D, two different configurations of the $Mo(CO)_3$PPP headgroup are possible after attachment to the SAM backbone (graphic depictions for **Click 3** and **4** are shown in Fig. S63†). The "head-up" orientation features an upright standing head group for all three preparation protocols **Click 1**, **Click 3** and **Click 4**, giving the headgroup access to the boundary layer (Fig. 7C and S63†). This is contrasted in the "head-down" configuration where all CO-ligands are oriented towards the surface (Fig. 7D and S63†). Notably, both geometries produce identical IRRA spectra and therefore are indistinguishable. It is plausible that both configurations are present on the surface due to the high flexibility of the Mo $(CO)_3$PPP fragment and its rotability around the phenylene and triazole moieties connecting the complex with the SAM-backbone. However, on a densely covered surface, steric interactions with the underlying SAM itself might limit this rotational freedom to some extent, making one of the two configurations energetically more favourable. To elucidate which configuration is dominant on the surface, we conducted geometry optimizations of a 4 × 4 fragment of **8-N_3SH**@Au(111) at the semi-empirical GFN-xTB1 level of theory, which is known to produce accurate geometries for larger molecules (Fig. 8).[124,125] Due to steric interactions with the terminating N_3-groups, the $Mo(CO)_3$-headgroup is tilted to the side and deposits itself onto the SAM-backbone. This is indicative for the "head up" rather the "head down" orientation in the standing-up phase of the SAM.

For all three successfully clicked samples, additional CO-stretching vibrations are present around 2020 and 1900 cm^{-1}, most visible for **Click 1** (Fig. 7B and S58, S59†). DFT calculations were conducted to determine whether these are spectroscopic features of a possible surface *mer*-isomer of **8** or, alternatively, possible $[Mo(CO)_2(PPP)]$ or $[Mo(CO)_2(PPP)]^+$ species resulting from CO loss (Fig. S70 and S71†). By comparing the corresponding calculated IR-spectra with the experimental IRRAS data for **Click 1**, the calculated CO-stretches for $[Mo(CO)_2(PPP)]$ as well as $[Mo(CO)_2(PPP)]^+$ are predicted to have lower frequencies (Fig. S72 and S73†). Additionally, the energy difference between the symmetric and antisymmetric CO-stretching vibrations is predicted to be around 42 cm^{-1} for $[Mo(CO)_2(PPP)]$, a lot smaller than the difference between the observed stretching vibrations (~120 cm^{-1}). The energy gap difference roughly doubles for $[Mo(CO)_2(PPP)]^+$, but is still below the observed value (Fig. 7B). We thus attribute the stretches around 2020 and 1900 cm^{-1} to the presence of a small amount of *mer*-isomer, which would be in line with the observed photoinduced isomerization of **8** in solution (see above).

Notably, there is a shift in peak maxima of 5–10 cm^{-1} ($A'_{(1)}$) and 8–12 cm^{-1} (A'') or 8–15 cm^{-1} ($A'_{(2)}$) to higher wavenumbers for **Click 1**, **Click 3** and **Click 4** (Fig. 6 and Fig. S58, S59†) compared to isotropic IR spectra of **8** (Fig. 3 and Fig. S60, S61†).

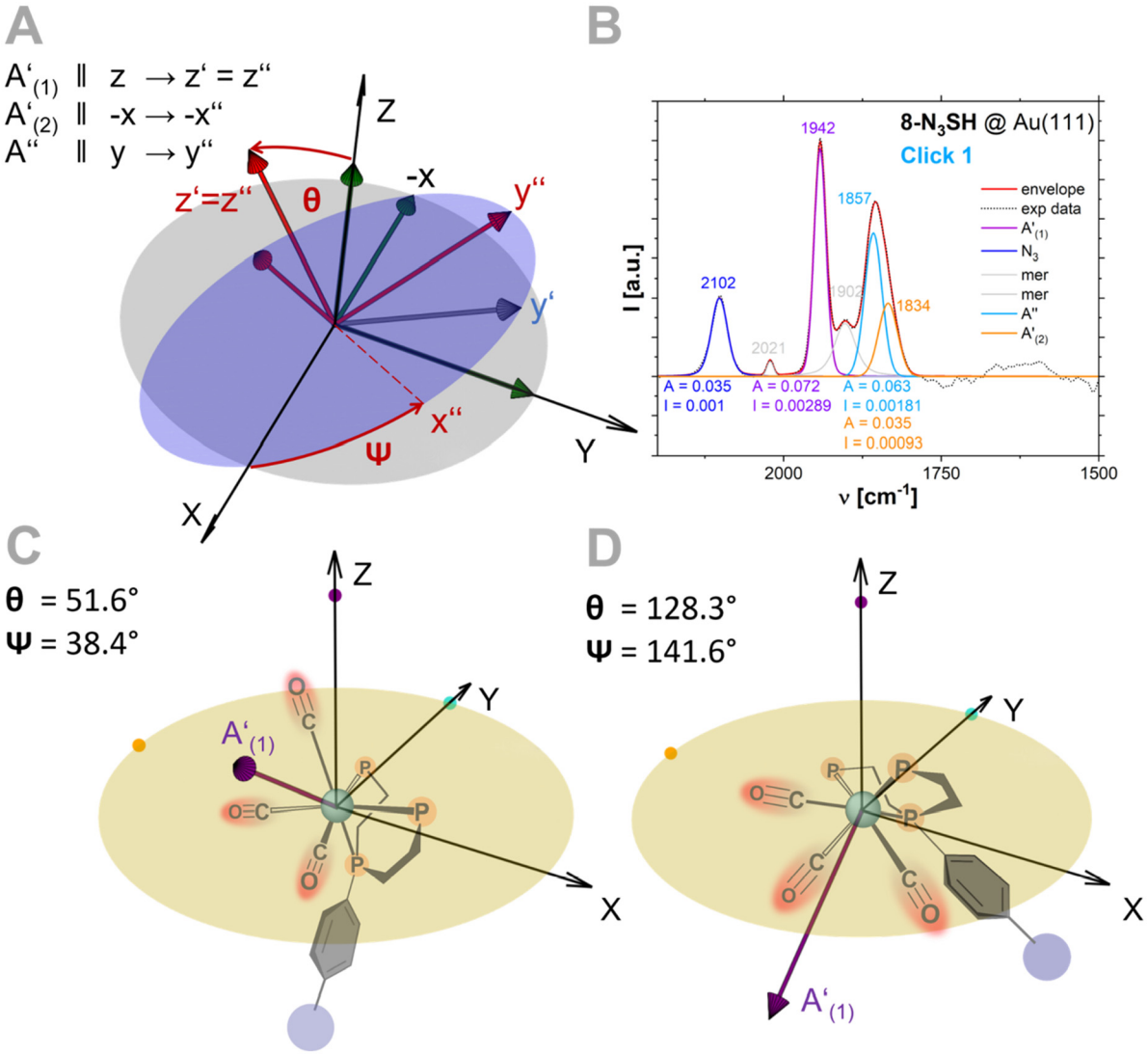

Fig. 7 (A) Schematic depiction of the utilized rotation angles θ and Ψ. At first, the TDM vectors $A'_{(1)}$, A'' and $A'_{(2)}$ are aligned to the laboratory frame X, Y, Z as $A'_{(1)}||Z$, $A''||Y$ and $A'_{(2)}||-X$. Rotation by the angle θ around the X-axis creates a new tilted molecular frame (blue) with the corresponding tilted TDM vectors (only y' is shown). The second rotation by the angle Ψ around Z' creates the final vector set depicted in red. (B) Fitted experimental IRRA-spectra of **Click 1** to obtain reliable intensities for all three CO stretches $A'_{(1)}$, A'' and $A'_{(2)}$ (*cf.* Table 4). (C) Resulting orientation of $A'_{(1)}$-TDM vector of the $Mo(CO)_3$PPP-head group in the "head up" configuration for **Click 1** protocol relative to the Au(111)–surface. (D) Resulting orientation of $A'_{(1)}$-TDM vector of the $Mo(CO)_3$PPP-head group in the "head down" configuration for **Click 1** protocol relative to the Au(111)–surface. The residual SAM backbone is indicated by the blue circle. Colored dots indicate the starting direction for each TDM relative to the laboratory coordinate system.

Table 3 Calculated values for $R_n = I_n^{SAM}/I_n^{Bulk}$, R_{yx} and R_{xz} as well as the resulting angles Ψ and θ for **Click 1**, **Click 3** and **Click 4**. For additional information refer to the ESI†

	Click 1		**Click 3**		**Click 4**	
R_x	9.161×10^{-3}		1.987×10^{-2}		4.078×10^{-3}	
R_y	1.456×10^{-2}		2.800×10^{-2}		7.973×10^{-3}	
R_z	1.487×10^{-2}		1.734×10^{-2}		5.789×10^{-3}	
R_{yx} (Ψ)	1.590		1.409		1.955	
R_{xz} (θ)	6.160×10^{-1}		1.146		7.045×10^{-1}	
Ψ	38.4°	141.6°	40.1°	139.8°	35.6°	144.4°
θ	51.6°	128.3°	59.0°	121.0°	55.2°	124.8°

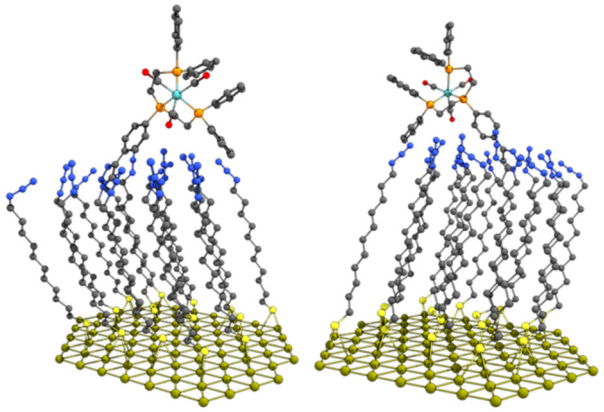

Fig. 8 Graphic depiction of a 4 × 4 fragment of **8-N_3SH**@Au(111) optimized at the GFN-xTB1 level utilizing ORCA 6.0.[124,137] All hydrogens are omitted for clarity.

Similar shifts were observed in our earlier studies dealing with physisorbed TATA-systems (Fig. 1, top), (Table 4).[45,46] Differences between bulk and monolayer CO-stretching vibrations were attributed to static and dynamic (de)-activation effects on the metallic surface, facilitated by the extended π-system of the deposited TATA-platforms. However, the shifts observed for **8-N_3SH**@Au(111) are significantly smaller. Apart from an electronic influence of the surface they may also be attributed to intrinsic optical effects caused by the grazing angle of incidence and different reflectivity values *k* and refractive indices *n* between the SAM and the substrate which is known for thin films.[115]

Electrochemistry of grafted complexes

To evaluate the surface coverage and overall effectiveness of the employed clicking method, CVs of **8-N_3SH**@Au(111) with Au working electrodes were recorded (Fig. 9 and S65–S67†). Oxidation of the $Mo(CO)_3$(PPP) moiety produces an irreversible peak at about 0.15 V *vs.* Fc/Fc^+ in THF/NBu_4PF_6, the exact potential depending on the employed catalyst. Presumably, the irreversibility of this process is due to CO loss during oxidation, as already found in homogenous solution (Fig. 4). A broad reductive wave is observed in the −1.25 to −1.75 V range (Fig. 9) which corresponds to Au–S cleavage of pure N_3SH@Au WE (Fig. S50†). Based on the oxidative peak area of **8-N_3SH**@Au(111) we calculated surface coverages of Γ_{Click} = 2.64 × 10^{-11} (**Click 1**), 1.10 × 10^{-10} (**Click 3**) and 1.06 × 10^{-10} mol cm^{-2} (**Click 4**). These values correspond to a degree of

Table 4 Comparison of wavenumber shifts between bulk material and surface for all the CO-stretching modes for **8-N_3SH**@Au(111), [Mo$(CO)_3$(TATA-P_3)]@Au(111)[46] and [Mo$(CO)_3$(PN^3P-TATA)]@Au(111)[45]

Bulk-IRRA	**8-N_3SH**	[Mo$(CO)_3$(TATA-P_3)]	[Mo$(CO)_3$(PN^3P-TATA)]
$\Delta A'_{(1)}$	5–10	26	8
$\Delta A''$	8–12	31	31
$\Delta A'_{(2)}$	8–15		36

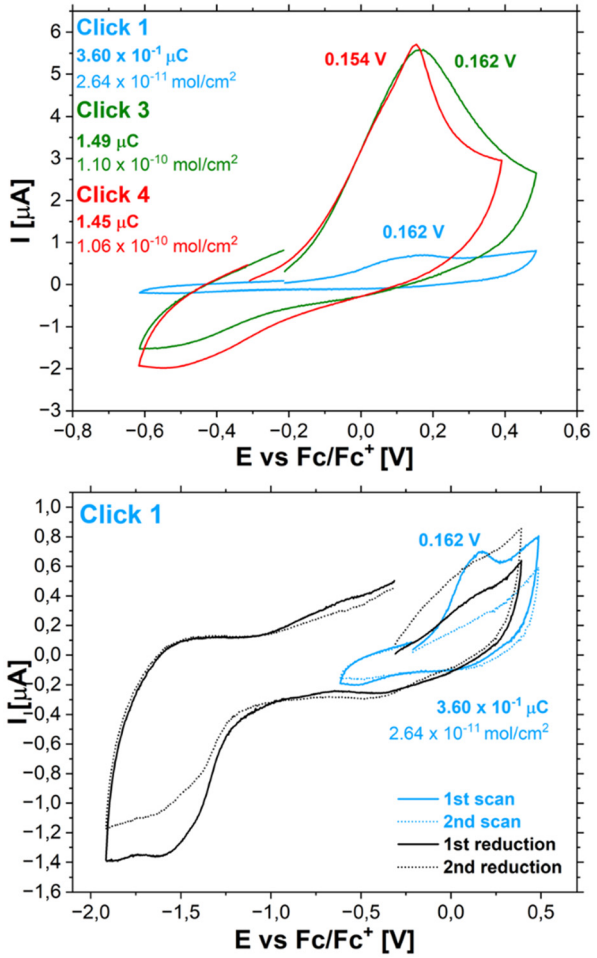

Fig. 9 Top: CVs of **8-N_3SH**@Au-WE prepared with the **Click 1** and **Click 3**, **4** protocols (1st experimental scan). Bottom: CVs of the 1st and 2nd oxidative scan (turquoise) in the redox-active region of **8**. Subsequent reductive scans (black) show a very broad reductive wave around −1.5 V corresponding the Au–S cleavage. Experimental data for **Click 3** and **Click 4** see Fig. S65–S67.†

functionalization of 3% (**Click 1**), 14% (**Click 3**) and 13% (**Click 4**) per available N_3-moiety and are in a similar order of magnitude as observed for comparable transition-metal containing SAMs on Au.[82,126] The surface coverage of a given area by close-packed $Mo(CO)_3$(PPP) fragments was estimated to be 66% based on its van der Waals volume (Fig. S65 and S66†). Additionally, we calculated the ratio between the observed number of complex fragments (*A*(exp)) and the number of complex fragments based on a close packing (*A*(calc)) per electrode surface $\frac{A(\exp)}{A(\mathrm{calc})}$, giving values of 0.289 (**Click 1**), 1.20 (**Click 3**) and 1.16 (**Click 4**). Values >1 imply twisting and stacking interactions between $Mo(CO)_3$(PPP) head groups to increase the surface coverage. One of the two possible configurations ("head-up", "head-down") might be favored over the other in this scenario. Consequently, orientation values for **Click 1** have to be interpreted differently compared to **Click 3** and **4**: a low surface coverage indicates very little steric inter-

actions between each functionalized head group. Therefore, the calculated rotational angles (θ, Ψ) may in fact reflect true molecular orientations on the surface. For **Click 3** and **Click 4**, steric interactions are present due to the high surface coverage, which may lead to a broader distribution of orientations around the mean values of the angles θ and Ψ. Strong molecular interactions between $Mo(CO)_3$(PPP) head groups could also explain the slightly different wave shapes observed for **Click 3** and **Click 4** (Fig. 9).

Despite similar Γ_{Click} values determined for **Click 3** and **Click 4**, the IRRAS intensity of the N_3-valence stretch at 2102 cm^{-1} is much lower for the former than for the latter (Fig. 6). A possible explanation for this observation lies in the Au–S interface of the respective samples: As indicated before, CuAAC leads to different regional S 2p XP-spectra for **Click 3** and **Click 4** (Fig. S54 and S55†). Especially oxidized sulphur species are associated with SAM-degradation[79,80] and are visible after the post-functionalization. The destruction of a more ordered standing-up phase of the SAM-backbone corresponds to a higher number of bent or even flatly absorbed molecules of **N_3SH**. As a result the intensity of the azide-stretching mode is greatly diminished in the IRRA-spectrum of **Click 3** compared to **Click 4**.

Finally, the intensity of azide-related signals may also be influenced by the employed substrates, which are vapor-deposited Au on SiO_2-wafers for XPS and IRRAS and classical 3 mm polished Au working electrodes for electrochemistry. All in all, **Click 1** and **Click 4** thus have been identified as the optimal protocols for immobilization of the title complex, depending on the targeted surface coverage (high for **Click 4**, low for **Click 1**).

Summary and conclusions

The synthesis of a new PPP-type ligand $etPP^{PhTMS}P$ **6** with an ethynyl moiety in the ligand-backbone has been described. Additionally, molybdenum carbonyl-complexes [$Mo(CO)_3(etPP^{PhTMS}P)$] **7** and [$Mo(CO)_3(etPP^{PhH}P)$] **8** have been synthesized and characterized by NMR- and IR- spectroscopy as well as electrochemistry, showing strong similarities with the parent complex [$Mo(CO)_3$(PPP)] (PPP = triphos). Hence, the influence of the ethynyl group on the electronic and geometric structure is small.

The chosen ligand design enables covalent attachment of transition-metal complexes onto surfaces *via* CuAAC. This concept has been demonstrated by coupling **8** to N_3-terminated SAMs on Au-surfaces, employing four different Cu-catalysts (**Click 1–4**). The resulting samples of **8-N_3SH**@Au(111) were investigated by XPS, IRRAS and CV. While **Click 2** based on the [$CuBr(PPh_3)_3$] catalyst did not lead to any functionalization, experimental data on **Click 1**, **3** and **4** confirmed successful surface attachment of the $Mo(CO)_3$(PPP) fragment with preservation of its molecular structure.

IRRAS was employed in order to determine the surface orientation of the molybdenum carbonyl head group. For the transition dipole moments of the three carbonyl stretching modes, polar- and azimuthal angles θ and Ψ have been determined and found to have similar values for **Click 1**, **Click 3** and **Click 4**. However, based on given values of θ and Ψ two different configurations of the head group are possible, "head-up" and "head-down". In the former case, the $Mo(CO)_3$-core is oriented towards the boundary layer and exhibiting a preferrable configuration in all three cases, but the latter orientation would impose steric barriers for potential applications of similar systems. Our exprimental and theoretical data suggests that the "head up" configuration represents the preferred orientation of the $Mo(CO)_3$-headgroup for the standing up phase of the SAM.

The overall surface coverage of the prepared samples was estimated based on CVs of **8-N_3SH** prepared on Au WEs and revealed a low functionalization degree of 3% for **Click 1** and higher values for **Click 3** (14%) and **Click 4** (13%). Due to the lower coverage, **Click 1** can be assumed to provide a more uniform surface compared to **Click 3** and **Click 4**, both of which produce surfaces densely covered with molybdenum tricarbonyl moieties. Comparing the last two methods, however, **Click 3** shows signs of decomposition of the underlying SAM whereas **Click 4** leaves the SAM intact. This may lead to a larger fraction of "head-down" molybdenum tricarbonyl groups in the case of **Click 3**, as steric interactions with the standing-up phase of the SAM are reduced. Altogether, **Click 4** based on $[Cu(MeCN)_4]PF_6$ in conjunction with 2,6-lutidine[109] thus has been found to be the most suitable method for the functionalization of the azide-terminated SAM leading to a dense layer of [$Mo(CO)_3(etPP^{PhH}P)$] complexes **8**.

Whereas electrochemical oxidation of **8** was found to be irreversible, the protocol developed in this paper can well be adapted to the immobilization of other redox-active transition-metal complexes on metallic surfaces. Moreover, the approach followed in this paper was based on gold, due to the favorable properties of this substrate with respect to chemical inertness and surface-spectroscopic characterization. However, the methods utilized herein can also be applied to other surfaces in combination with suitable linkers. A possible substrate would be glassy carbon which can also be functionalized *via* the click reaction, using, *e.g.*, azide-functionalized diazonium salts.[127–129] This would render the resulting surface layers chemically and electrochemically more stable than sulphur-based SAMs, which in turn would be beneficial for applications of such systems in, *e.g.*, electrocatalysis.

Experimental section

General synthetic procedures

Commercially available starting materials and solvents were purchased from Sigma-Aldrich Co. LLC, abcr GmbH, Deutero and Fisher Scientific in reagent grade and were used as received. Water and oxygen-sensitive reagents were handled in a M. Braun Labmaster 130 Glovebox under N_2. All reactions were performed under Ar- or N_2-atm. by using standard

Schlenk techniques if not stated otherwise. [$Mo(CO)_3$(cht)] was prepared according to published procedures.[130,131] 1-Azido-11-undecanethiol (**N_3SH**) has been prepared adapting published procedures.[102,132] Solvents were dried with $LiAlH_4$ (Et_2O), potassium (THF) and CaH_2 (toluene, *n*-pentane, DCM) under Ar and distilled prior to use. EtOH and MeOH were dried with CaH_2 (EtOH) and Mg (MeOH), distilled under Ar and stored over 3 Å molecular sieves under Ar- and N_2-atm, respectively.

NMR spectroscopy

The NMR spectra were recorded in deutered solvents at 300 K using a Bruker Avance 400 Puls Fourier Transform spectrometer [^{1}H NMR (400.13 MHz), ^{13}C NMR (101 MHz), ^{31}P NMR (161.98 MHz)]. Referencing was performed either suing the solvent residue signal [7.26 ppm for $CDCl_3$, 5.32 ppm for CD_2Cl_2, 3.58 ppm for thf-d_8 and 7.16 ppm for C_6D_6] or TMS [δ^1H = 0 ppm]. ^{31}P NMR spectra were referenced to H_3PO_4 85% [$\delta(^{31}P)$ = 0 ppm] as a substitutive standard.

IR spectroscopy

The IR spectra were recorded at room temperature with a Bruker Alpha-P ATR-IR Spectrometer. Additional spectra were recorded using a Bruker Vertex70 FT-IR spectrometer using a broadband spectral range extension VERTEX FM for full mid and far IR in the range of 6.000–80 cm^{-1}.

Elemental analysis

The elemental analyses were measured using a Euro Vector CHNS-O element analyser (Euro EA 3000): the prepared assays in tin vessels were burnt in a stream of oxygen.

Single crystal structure determination

The data collections were performed using a XtaLAB Synergy, Dualflex, HyPix diffractometer with $Cu_{K\alpha}$ radition (λ = 1.546 Å). The structures were solved with SHELXT[133] and refined with SHELXL[134] using Least Squares minimisation. All non-hydrogen atoms were refined anisotropic. The C–H H atoms were positioned with idealized geometry (methyl H atoms allowed to rotate but not to tip) and were refined isotropic with U_{iso}(H) = 1.2 U_{eq}(C) (1.5 for methyl H atoms) using a riding model. For compound **6**·$(BH_3)_3$ The B–H H atoms were located in difference map and were refined isotropic with varying coordinates. The asymmetric unit of compound **7** and **8** consists of two crystallographically independent complexes. The structure of compound **8** contain half of a tetrahydrofurane molecule per formula units that is disordered. Because no reasonable structure model was found its contribution to the electron density map was removed. CCDC 2452994 (**6**·$(BH_3)_3$), CCDC 2452996 (**7**) and CCDC 2452995 (**8**) contain the supplementary crystallographic data for this paper.†

Electrochemistry

Electrochemical studies were performed in a glovebox (Jacomex) (O_2 < 1 ppm, H_2O < 1 ppm) with a home-made 3-electrode cell (WE: Au, Pt or glassy carbon, RE: Ag-wire in a 1 mM Fc^+/Fc, 0.1 M $TBAPF_6$ in THF, DCM or MeCN solution, CE: Pt-wire). Ferrocene was added at the end of the experiments to determine the exact redox potential values. Measurements in aqueous media were performed using an AUTOLAB PGSTAT 100 (Metrohm). Additional measurements were performed in an Inertec AG glovebox (ITA 14 Spez.) under N_2-Atm. (O_2 < 1 ppm) using a custom made 3-electrode cell. The applied potential for these measurements was controlled by an AUTOLAB PGSTAT204 (Metrohm). Both potentiostats were monitored by the Metrohm NOVA © software. The working electrodes (d = 3 mm) were polished over a 1 μm alumina slurry, rinsed with water, sonicated in H_2O and acetone, then dried in a stream of N_2. Electrodes were transferred directly into a glovebox. Au-electrodes were electrochemically polished according to the literature[135,136] by cycling between 0.6 and 1.6 V (*vs.* Ag/AgCl) for a minimum of 50 and up to 80 scans in 0.1 M H_2SO_4 until the current signal was stable. The procedure was always stopped at a potential value more negative than gold oxide reduction (*i.e.* 0.6 V). Au-electrodes were thoroughly rinsed with EtOH and used for further functionalization.

Gold substrates

For the IRRAS measurements glass substrates with a 50 Å titanium adlayer and a 200 nm evaporated gold film from EMF corporation (Ithaca, NY) were used. XPS and NEXAFS measurements were undertaken on sputtered Au/Cr/Si wafers (Au 206 nm, Cr 8 nm).

Preparation of (functionalized) monolayers

Clean Au-substrates were immersed in a 5 mM solution of 1-azido-11-undecanethiol **N_3SH** in abs. EtOH for at least 48 h while keeping exposure to light to a minimum under Ar- or N_2-Atm. Samples were rinsed with copious amounts of absolute EtOH under inert-Atm, transferred into screwable tubes and treated in an ultrasonic bath for 3 min to remove physisorbed species. Afterwards, the azide terminated Au-substrates were rinsed again and put under inert atmosphere in a glovebox. This procedure was carried out as quickly as possible to limit possible air exposure. The wafers were placed in a glass vessel of appropriate dimensions and filled with 1/3 of a 1 mM solution of complex **8** in distilled THF, 1/3 of a click solution of choice and 1/3 with abs. MeOH. The vessels were stored under inert atmosphere at room temperature for up to 2 h while keeping exposure to light to a minimum. Afterwards, the grafted substrates were rinsed with 10 mL (5 mL for small wafers) distilled THF and 20 mL (10 mL) absolute MeOH and treated in an ultrasonic bath for 3 min to remove physisorbed species (inert atm.) The wafers were washed with 20 mL (10 mL) abs. MeOH again and were dried under a stream of nitrogen. All samples were transferred to the measurement chamber directly and under inert atm. A similar procedure was used when working with conventional Au-electrodes.

IRRAS

Measurements were executed by using a Bruker VERTEX 70 FTIR spectrometer equipped with a polarisation modulation

accessory (PMA) 50 unit (Bruker Optik GmbH, Ettlingen, Germany) and a liquid-nitrogen-cooled MCT detector in a horizontal reflection unit for grazing incidence (Bruker A518). Before, as well as during measurements the sample chamber was purged with dry nitrogen and for the background spectrum a hexadecanethiol SAM on Au(111) was used as a reference for conventional IRRA spectra. A p-polarised beam at an incident angle of 80° to the surface normal was used for the measurements. The resolution of all recorded spectra amounted to 4 cm^{-1} resolution and each spectrum contains 2048 averaged spectra. The processing of the IRRAS data was carried out using the OPUS software Version 6.5 (Bruker, Germany). Area calculations for specific absorption bands were performed in OPUS 6.5 after removal of atmospheric components (CO_2, H_2O) from the experimental spectra. Baseline correction of the resulting IRRAS data was performed by the rubber band method in an interactive mode and resulted data was smoothed slightly before plotting.

XPS

The XPS data was recorded at the BESSY II synchrotron radiation facility at the beamline HE-SGM using the PREVAC end station. The experimental station provides a hemispherical VG Scienta R3000 photoelectron analyser. With its 150 nm slits the energy resolution $E/\Delta E$ of the beamline amounts to 800. While the XP survey spectra were recorded at 700 eV photon energy by using an analyser pass energy of 100 eV, the region XP spectra were acquired with the following excitation energies: 350 eV for C 1s, Mo 3d, P 2p and S 2p and 500 eV for N 1s spectra by using an analyser pass energy of 50 eV. The processing of the XP spectra was performed with the program CASA XPS. To define the relative compensation of the adlayers, the XP spectra were energy-corrected by using the Au $4f_{7/2}$ line at a binding energy of 84.0 eV as a reference. A background correction was carried out with the combination of a Shirley background for all the signals. The fitting parameters are listed in Tables S9, S10, S11, S12 and S13 of the ESI.†

Computational methods

All calculations were done using ORCA 6.0.[137,138] Gasphase optimizations of **8-N_3SH**, **[Mo(CO)$_2$(PPP)]** and **[Mo(CO)$_2$(PPP)]$^+$** were done at the PBE0 level of theory using def2-TZVP basis set with D3BJ correction and RIJCOSX approximation.[139,140] A fine grid (DEFGRID3) was employed and final geometries were confirmed by the appropriate number of negative frequencies (zero). The surface model of **8-N_3SH**@Au(111) was modeled by first optimizing the 4 × 4 fragment of the SAM at the PBE0 def2-SVP level in the gasphase. The resulting structure was employed as starting geometry for the final optimization step on a single sheet of gold atoms using Grimme's GFN-xTB1 functional.[124,125] Final coordinates are given in the ESI.†

Divinyldiethylaminophosphine (vinyl)$_2$PNEt$_2$ (2)

In a Schlenk flask 5.57 g (32.0 mmol, 1 eq.) diethylaminedichlorophosphine **1** was put under N_2-atm. *via pump freeze thaw* technique, dissolved in 40 mL abs. THF and subsequently cooled to −96 °C. Next, 64 mL (64.0 mmol, 2 eq.) of a 1 M solution of vinylmagnesiumbromide **2** were added dropwise over the span of 1 h to the stirring solution at −96 °C. The mixture was allowed to heat up to ambient temperature and stirred for additional 12 h. The reaction was quenched by addition of 100 mL abs. *n*-pentane and filtered *via* a Schlenk frit to remove solids from the mixture. The yellow filtrate was removed *in vacuo* and collected separately. The clear solution was distilled at atm. pressure under N_2-atm. to remove THF and *n*-pentane (T_{max} = 90–100 °C). *Note: Distillation should not be carried out above 100 °C. Product tends to decompose at high temperatures and contains quite some amount of THF. Ratio of the THF/product mixture was calculated by ^{1}H NMR integrals.* The product was obtained as yellowish liquid in a remaining amount of THF: 3.70 g (23.8 mmol, 74%). ^{1}H NMR (400 MHz, 300 K, $CDCl_3$): δ = 6.05 (ddd, $^2J_{H-P}$ = 17.8 Hz, $^3J_{H-Htrans}$ = 18.5, $^3J_{H-Hcis}$ = 12.1 Hz, 2 H, C*H*), 5.40 (ddd, $^3J_{H-P}$ = 26.3, $^3J_{H-Hcis}$ = 12.1 Hz, $^2J_{H-H}$ = 2.3 Hz, 2 H, CH_2), 5.24 (ddd, $^3J_{H-Htrans}$ = 18.5 Hz, $^3J_{H-P}$ = 11.5 Hz, $^2J_{H-H}$ = 2.3 Hz, 2 H, CH_2), 2.72 (dq, J = 9.7, 7.1 Hz, 4 H, CH_2), 0.77 (t, J = 7.1 Hz, 6 H, CH_3) ppm. ^{31}P{^{1}H}-NMR (162 MHz, 300 K, $CDCl_3$): δ = 53.40 (s, 1 P, *P*) ppm. ^{13}C{^{1}H}-NMR (100 MHz, 300 K, $CDCl_3$): δ = 138.90 (d, $^1J_{C-P}$ = 17.1 Hz, 2 C, *C*H), 123.70 (d, $^2J_{C-P}$ = 19.9 Hz, 2 C, *C*H_2), 43.33 (d, $^2J_{C-P}$ = 14.2 Hz, 2-C, *C*H_2), 14.49 (d, $^3J_{C-P}$ = 3.5 Hz, 2-C, *C*H_3) ppm.

Bis-ethyldiphenylphosphin-diethylaminophosphine, etPP^{NEt2}P (3)

A solution of 3.70 g (23.8 mmol, 1 eq.) of divinyldiethylaminophosphine **2** in 10 mL abs. THF was prepared under N_2-atm. in a schlenk flask. Subsequently, 9.22 g (49.5 mmol, 2.1 eq.) $HPPh_2$ and two spatula (150–200 mg) of KH were added slowly while stirring. The suspension was stirred for 20 min at rt before transferring onto a reflux condenser. The mixture was then refluxed for 5 d under N_2-atm. before addition of 20 mL abs. Et_2O. The organic phase was washed with 5 mL degassed H_2O five times, dried over $MgSO_4$ and filtered under inert atm. Solvents were removed *in vacuo* to yield the product **3** as a colorless oil that crystalized over the span of a few days to yield a colorless solid: 11.3 g (21.3 mmol, 89%). *Note: Excess $HPPh_2$ can be removed at 10^{-2} mbar and 160 °C if necessary.* EA (exp/*calc*): C (72.32/*72.58*), H (7.10/*7.23*), N (2.27/*2.64*) %. ^{1}H NMR (400 MHz, 300 K, CD_2Cl_2): δ = 7.42–7.36 (m, 12 H, P*Ph*$_2$), 7.22–7.39 (m, 8 H, P*Ph*$_2$), 2.84 (dq, $^3J_{H-P}$ = 8.9 Hz, $^3J_{H-H}$ = 7.1 Hz, 4 H, CH_2), 2.11–2.02 (m, 4 H, CH_2), 1.55–1.41 & 1.16–1.03 (m, 4 H, CH_2), 0.96 (t, $^3J_{H-H}$ = 7.1 Hz, 6 H, CH_3) ppm. ^{31}P{^{1}H}-NMR (162 MHz, 300 K, CD_2Cl_2): δ = 61.16 (t, $^3J_{P-P}$ = 31.6 Hz, 1 P, *P*Et$_2$), −11.99 (d, $^3J_{P-P}$ = 31.6 Hz, 2 P, *P*Ph$_2$) ppm. ^{13}C{^{1}H}-NMR (100 MHz, 300 K, CD_2Cl_2): δ = 139.07 (d, $^1J_{C-P}$ = 14.69 Hz, 2 C, *C*), 139.00 (d, $^1J_{C-P}$ = 14.69 Hz, 2 C, *C*), 132.82 (d, $^2J_{C-P}$ = 3.5 Hz, 4 C, *C*H-*arom*), 132.6 (d, $^2J_{C-P}$ = 3.3 Hz, 4 C, *C*H-*arom*), 128.55 (d, $^3J_{C-P}$ = 2.1 Hz, 4 C, *C*H-*arom*), 128.46 (d, $^3J_{C-P}$ = 1.7 Hz, 4 C, *C*H-*arom*), 128.40 (d, $^3J_{C-P}$ = 1.8 Hz, 4 C, *C*H-*arom*), 42.9 (d, $^2J_{C-P}$ = 14.1 Hz, 2 C, *C*H_2), 25.6 (dd, $^1J_{C-P}$ = 17.2 Hz, $^2J_{C-P}$ = 13.9 Hz, 2 C, *C*H_2), 23.7 (dd, $^1J_{C-P}$ = 17.0 Hz, $^2J_{C-P}$ = 13.4 Hz, 2 C, *C*H_2), 15.3 (d, $^3J_{C-P}$ = 2.5 Hz, 2 C, *C*H_3) ppm.

Bis-ethyldiphenylphosphin-chlorophosphine, etPP^{Cl}P (4)

A solution of 250.1 mg (47.2 μmol, 1 eq.) etPP^{NEt2}P **3** in 10 mL abs. Et_2O was prepared in a schlenk flask under N_2-atm. Adding 0.59 mL (1.18 mmol, 2.5 eq.) of a 2 M HCl-solution in Et_2O leads to the formation of a white precipitate. The suspension was stirred overnight under inert atm. before filtration *via* Schlenk frit (no external vacuum). *Note: Although precipitation of the ammonium salt is immediate it is recommonded to stir the suspension for at least 10 h.* The precipitate was washed with additional 5 mL abs. Et_2O and discarded. The filtrate was dried *in vacuo* to yield etPP^{Cl}P **4** as a colorless oil. Yield: 209 mg (42.3 μmol, 90%). *Note: etPP^{Cl}P tends to decompose after several days even if stored under N_2-atm. and therefore should be quickly processed.* ^{1}H NMR (400 MHz, 300 K, CD_2Cl_2): δ = 7.33–7.27 (m, 8 H, P*Ph*$_2$), 7.25–7.20 (m, 12 H, P*Ph*$_2$), 2.15–2.06 (m, 4 H, C*H*$_2$), 1.84–1.74 (m, 4 H, C*H*$_2$) ppm. ^{31}P{^{1}H}-NMR (162 MHz, 300 K, $CDCl_3$): δ = 114.51 (t, $^3J_{P-P}$ = 28.5 Hz, 1 P, *P*Et$_2$), −13.56 (d, $^3J_{P-P}$ = 28.5 Hz, 2 P, *P*Ph$_2$) ppm. ^{13}C{^{1}H}-NMR (100 MHz, 300 K, $CDCl_3$): δ = 138.03 (d, $^1J_{C-P}$ = 14.1 Hz, 4 C, *C*), 132.84 (s, 4 C, *C*H-*arom*), 132.66 (s, 4 C, *C*H-*arom*), 128.90 (s, 4 C, *C*H-*arom*), 128.64 (s, 4 C, *C*H-*arom*), 128.57 (s, 4 C, *C*H-*arom*), 30.09 (dd, $^1J_{C-P}$ = 33.0 Hz, $^2J_{C-P}$ = 16.0 Hz, 2 C, *C*H$_2$), 22.27 (dd, $^1J_{C-P}$ = 14.8 Hz, $^2J_{C-P}$ = 11.9 Hz, 2 C, *C*H$_2$) ppm.

Bis-ethyldiphenylphosphin-trimethylsilylethynylphenylphosphine etPP^{PhTMS}P (6)

A solution of 905.0 mg (3.57 mmol, 1 eq.) 1-Bromo-4-trimethylsilylethynylbenzene **5** in 10 mL abs. THF was prepared in a schlenk flask and cooled to −96° C. Dropwise addition of 1.43 mL (3.57 mmol, 1 eq.) 2.5 M *n*-butyllithium solution in *n*-hexane and subsequent stirring for 2 h at −96 °C resulted in formation of an orange reaction mixture. After dropwise addition of freshly prepared 1.90 g (3.58 mmol, 1 eq.) etPP^{Cl}P **4** in 15 mL abs. THF *via* a drip funnel over a duration of 30 min and subsequent stirring for additional 2 h at −96 °C, the cooling bath was removed to enable stirring at rt for 3 d. The volume was reduced to 5–10 mL *in vacuo* before addition of 15 mL abs. diethylether with 5 mL degassed H_2O and stirred for 5 min. Phase separation was accomplished *via* syringe before filtration on silica in a schlenk frit with abs. diethylether. The solvent was removed *in vacuo* to yield the crude product as yellow-white solid. Yield: 1.88 g (84%). EA (exp/*calc*): C (74.53/*74.26*), H (6.80/*6.55*) %. ^{1}H NMR (400 MHz, 300 K, CD_2Cl_2): δ = 7.39–7.35 (m, 2 H, P*Ph*), 7.31–7.28 (m, 20 H, P*Ph*), 7.26–7.23 (m, 2 H, P*Ph*), 2.02–1.85 (m, 4 H, C*H*$_2$), 1.74–1.65 (m, 4 H, C*H*$_2$), 0.25 (s, 9 H, SiC*H*$_3$) ppm. ^{31}P{^{1}H}-NMR (162 MHz, 300 K, CD_2Cl_2): δ = −12.94 (d, $^3J_{P-P}$ = 28.4 Hz, 2 P, *P*Ph$_2$), −16.24 (dd, $^3J_{P-P}$ = 29.2, 27.8 Hz, 1 P, *P*Et$_2$) ppm. ^{13}C{^{1}H}-NMR (100 MHz, 300 K, CD_2Cl_2): δ = 139.22 (d, $^1J_{C-P}$ = 19.2 Hz, 1 C, q*C*), 138.99 (d, $^1J_{C-P}$ = 24.5 Hz, 2-C, qC P*Ph*$_2$), 138.84 (d, $^1J_{C-P}$ = 24.5 Hz, 2-C, qC P*Ph*$_2$), 133.18 (t, $^2J_{C-P}$ = 18.3 Hz, 6-C, *C*H-*arom*), 132.75 (d, $^2J_{C-P}$ = 18.3 Hz, 4-C, *C*H-*arom*), 132.18 (s, 2-C, *C*H-*arom*), 132.12 (s, 2-C, *C*H-*arom*), 129.18 (d, *J* = 9.7 Hz, 2-C, *C*H-*arom*), 128.97 (d, $^3J_{C-P}$ = 6.7 Hz, 8-C, *C*H-*arom*), 124.14 (s, 1-C, qC *Ph*-C≡CH), 105.85 (s, 1-C, *C*≡CH), 95.52 (s, 1-C, C≡*C*H), 24.54 (t, 2 C, *C*H$_2$), 23.96 (t, 2 C, *C*H$_2$), 0.23 (s, 3 C, *C*H$_3$) ppm.

6 was crystallized as BH_3 protected **6**·$(BH_3)_3$ and its structure was defined by SC-XRD (*cf.* ESI†).

Synthesis of [Mo(CO)$_3$(etPP^{PhTMS}P)] (7)

A solution of 300 mg (1 eq.) etPP^{PhTMS}P **6** was dissolved in 15 mL of abs. THF and stirred at 50 °C under N_2-atm. Thereafter, a solution of 149 mg (1 eq.) [Mo(CO)$_3$(cht)] in 15 mL abs. *n*-Pentane was prepared in a schlenk flask, transferred into a cannula and added to **6** very fast. *During preparation and addition any light source was carefully excluded since [Mo(CO)$_3$(cht)] is sensitive to light in solution.* Following addition the solution was stirred for 2.5 h at 50 °C under N_2-atm. The yellow solution was filtrated and transferred *via* canulla to remove precipated impurities. The yellow solution was reduced under vacuum to give [Mo(CO)$_3$(etPP^{PhTMS}P)] **7** as yellow powder in 90% yield (347.0 mg). EA (exp/*calc*): C (61.94/*62.22*), H (5.34/*5.10*) %. ^{1}H NMR (400 MHz, 300 K, CD_2Cl_2): δ = 7.81–7.75 (m, 2 H, C*H arom.*), 7.60–7.55 (m, 4 H, C*H arom.*), 7.54–7.50 (m, 2 H, C*H arom.*), 7.32–7.27 (m, 4 H, C*H arom.*), 7.21–7.15 (m, 5 H, C*H arom.*), 7.14–7.09 (m, 3 H, C*H arom.*), 7.00–6.94 (m, 4 H, C*H arom.*), 2.74–2.41 (m, 4 H, C*H*$_2$), 2.09–1.80 (m, 4 H, C*H*$_2$), 0.25 (s, 9 H, C*H*$_3$) ppm. ^{31}P{^{1}H}-NMR (162 MHz, 300 K, CD_2Cl_2): δ = 83.30 (t, $^3J_{P-P}$ = 3.0 Hz, 1 P, *Pc*), 57.37 (d, $^3J_{P-P}$ = 3.2 Hz, 2 P, *P*Ph$_2$) ppm. ^{13}C{^{1}H}-NMR (100 MHz, 300 K, CD_2Cl_2): δ = 225.7 (dt, $^2J_{C-P}$ = 28.5 Hz, 9.6 Hz, 1 C, CO), 221.70–221.7–221.0 (m, 2 C, CO), 140.55–140.0 (m, 2 C, q*C*), 138.5–137.9 (m, 3 C, q*C*), 133.4–133.1 (m, 8 C, *C*H-*arom.*), 132.6–132.4 (m, 2 C, *C*H-*arom.*), 132.2–131.9 (m, 2 C, *C*H-*arom.*), 130.4 (s, 2 C, *C*H-*arom.*), 130.1 (s, 2 C, *C*H-*arom.*), 129.7–129.4 (m, 8 C, *C*H-*arom.*), 126.5 (s, 1 C, q*C*), 105.3 (s, 1 C, *C*≡CH), 97.6 (s, 1 C, C≡*C*H), 30.8–30.3 (m, 2 C, *C*H$_2$), 29.0–28.6 (m, 2 C, *C*H$_2$), 2.1 (s, 3 C, *C*H$_3$) ppm. ESI-MS: 812.11 *m*/*z*. IR (300 K): ν = 3051 (w), 2959 (m), 2921 (m), 2854 (w), 2155 (w, C≡C), 2017 (w), 1933 (vs, C≡O), 1850 (vs, C≡O), 1826 (vs, C≡O), 1586 (w), 1572 (w), 1482 (s), 1433 (s), 1414 (m), 1331 (w), 1304 (w), 1259 (s), 1249 (s), 1184 (m), 1157 (w), 1092 (s), 1016 (s), 859 (s), 841 (s), 798 (s), 737 (s), 692 (vs), 663 (s), 616 (s), 579 (s), 508 (s) cm^{-1}. Raman (300 K): ν = 3143 (w), 3058 (s), 3002 (w), 2960 (m), 2902 (s), 2850 (w), 2158 (vs, C≡C), 2019 (w), 1933 (w, CO), 1847 (s, CO), 1592 (vs), 1484 (w), 1434 (w), 1411 (w), 1263 (w), 1222 (m), 1187 (m), 1159 (w), 1097 (m), 1029 (m), 1000 (s), 825 (w), 761 (w), 698 (w), 665 (w), 619 (m), 518 (w) cm^{-1}.

Synthesis of [Mo(CO)$_3$(etPP^{PhH}P)] (8)

In a Schlenk flask 123 mg (0.151 mmol, 1 eq.) of **7** together with 16.1 mg (0.287 mmol, 1.9 eq.) KOH were dissolved in 8 mL abs. THF and 8 mL abs. MeOH and stirred for 2.5 h at 50 °C under N_2-atm. After cooling to ambient temperature the suspension was filtered through Celite over a Schlenk frit and washed with abs. THF until the filtrate became colorless. The clear yellow solution was removed *in vacuo* to yield 80 mg (72%) of **8** as yellow solid. ^{1}H NMR (400 MHz, 300 K, CD_2Cl_2): δ = 7.84–7.78 (m, 2 H, C*H arom.*-6), 7.61–7.54 (m, 4 H, C*H*

arom.-15, 5), 7.34–7.26 (m, 7 H, C*H arom.*-15/16/17), 7.22–7.15 (m, 4 H, C*H arom.*-15/16/17), 7.14–7.09 (m, 3 H, C*H arom.*-15/16/17), 7.00–6.94 (m, 4 H, C*H arom.*-15/16/17), 3.23 (s, 1 H, C≡C–*H*-1), 2.74–2.43 (m, 4 H, C*H2-11/12*), 2.09–1.85 (m, 4 H, C*H2-11/12*) ppm. $^{31}P\{^1H\}$-NMR (162 MHz, 300 K, CD_2Cl_2): δ = 82.9 (t, $^3J_{P-P}$ = 3.1 Hz, 1 P, *Pc*), 55.25 (d, $^3J_{P-P}$ = 3.1 Hz, 2 P, *P*Ph2) ppm. $^{13}C\{^1H\}$-NMR (100 MHz, 300 K, CD_2Cl_2): δ = 223.2 (dt, $^2J_{C-P}$ = 28.5 Hz, 9.4 Hz, 1 C, CO), 219.2–218.6 (m, 2 C, CO), 137.3–136.7 (m, 2 C, *qC-arom.*-7/14), 135.7–135.2 (m, 1 C, *qC-arom.*-7/14), 135.1–134.6 (m, 2 C, *qC-arom.*-7/14), 130.3–129.9 (m, 8 C, *C*H-*arom.*-15), 129.31–129.13 (m, 2 C, *C*H-*arom.*-17), 128.9–128.7 (m, 2 C, *C*H-*arom.*-17), 127.1 (s, 2 C, *C*H-*arom.*-6), 126.8 (s, 2 C, *C*H-*arom.*-5), 126.4–126.2 (m, 8 C, *C*H-*arom.*-16), 122.1 (s, qC, *C*-4), 80.8 (s, qC, *C*≡CH-3), 76.9 (s, qC, C≡*C*H-2), 27.5–27.1 (m, 2 C, *C*H_2-11/12), 25.7–25.2 (m, 2 C, *C*H_2-11/12) ppm. ESI-MS: 741.07 *m*/*z*. IR (300 K): ν = 3287 (w, CH-stretch (C≡C)), 3074 (w), 3052 (w), 2950 (w), 2927 (w), 2019 (m), 1933 (vs, CO), 1843 (s, CO), 1833 (vs, CO), 1586 (w), 1572 (w), 1482 (m), 1433 (m), 1414 (m), 1394 (w), 1378 (w), 1329 (w), 1306 (w), 1274 (w), 1249 (w), 1180 (m), 1159 (w), 1094 (m), 1069 (w), 1026 (w), 998 (w), 824 (w), 814 (w), 739 (m), 692 (m), 665 (w), 614 (w), 581 (s), 541 (w), 508 (s) cm^{-1}. Raman (300 K): ν = 3058 (s), 2958 (w), 2937 (w), 2908 (w), 2109 (vs), 2021 (w), 1851 (CO), 1841 (CO), 1594 (s), 1589 (s), 1573 (m), 1488 (w), 1434 (w), 1413 (w), 1268 (w), 1203 (w), 1184 (m), 1159 (m), 1095 (m), 1029 (m), 1001 (s), 782 (w), 680 (w), 619 (m), 518 (w) cm^{-1}.

Conflicts of interest

There are no conflicts to declare.

Data availability

The data supporting this article have been included as part of the ESI.†

Acknowledgements

The authors would like to thank the DAAD and SEA-EU program for funding. Additional thank goes to the HE-SGM staff at HZB BESSY II.

References

1 W. Grünert, W. Kleist and M. Muhler, *Catalysis at surfaces*, De Gruyter, Berlin, Boston, 2023.
2 J. Hagen, *Industrial catalysis. A practical approach*, Wiley-VCH, Weinheim, 2015.
3 L. Sévery, J. Szczerbiński, M. Taskin, I. Tuncay, F. Brandalise Nunes, C. Cignarella, G. Tocci, O. Blacque, J. Osterwalder, R. Zenobi, *et al.*, *Nat. Chem.*, 2021, **13**, 523.
4 S. Ren, D. Joulié, D. Salvatore, K. Torbensen, M. Wang, M. Robert and C. P. Berlinguette, *Science*, 2019, **365**, 367.
5 *Studies in Surface Science and Catalysis*, ed. T. J. Pinnavaia, A. Sayari and M. Jaroniec, Elsevier, 2000.
6 C. Copéret, A. Comas-Vives, M. P. Conley, D. P. Estes, A. Fedorov, V. Mougel, H. Nagae, F. Núñez-Zarur and P. A. Zhizhko, *Chem. Rev.*, 2016, **116**, 323.
7 M. K. Samantaray, E. Pump, A. Bendjeriou-Sedjerari, V. D'Elia, J. D. A. Pelletier, M. Guidotti, R. Psaro and J.-M. Basset, *Chem. Soc. Rev.*, 2018, **47**, 8403.
8 L. Sun, V. Reddu, A. C. Fisher and X. Wang, *Energy Environ. Sci.*, 2020, **13**, 374.
9 T. E. Rosser, M. A. Gross, Y.-H. Lai and E. Reisner, *Chem. Sci.*, 2016, **7**, 4024.
10 H. Roithmeyer, L. Sévery, T. Moehl, B. Spingler, O. Blacque, T. Fox, M. Iannuzzi and S. D. Tilley, *J. Am. Chem. Soc.*, 2024, **146**, 430.
11 K. U. Clausen, X. Meng, K. Reisig, C. Näther, T. Strunskus, R. Berndt and F. Tuczek, *J. Chem. Soc., Dalton Trans.*, 2024, 18304.
12 D. Evrard, F. Lambert, C. Policar, V. Balland and B. Limoges, *Chemistry*, 2008, **14**, 9286.
13 J. P. Collman, A. Dey, Y. Yang, S. Ghosh and R. A. Decréau, *Proc. Natl. Acad. Sci. U. S. A.*, 2009, **106**, 10528.
14 N. E. Leadbeater and M. Marco, *Chem. Rev.*, 2002, **102**, 3217.
15 M. Wang, K. Torbensen, D. Salvatore, S. Ren, D. Joulié, F. Dumoulin, D. Mendoza, B. Lassalle-Kaiser, U. Işci, C. P. Berlinguette, *et al.*, *Nat. Commun.*, 2019, **10**, 3602.
16 C. Vericat, M. E. Vela, G. Benitez, P. Carro and R. C. Salvarezza, *Chem. Soc. Rev.*, 2010, **39**, 1805.
17 T. Belser, M. Stöhr and A. Pfaltz, *J. Am. Chem. Soc.*, 2005, **127**, 8720.
18 B. Zhang and L. Sun, *Chem. Soc. Rev.*, 2019, **48**, 2216.
19 G. Grelaud, N. Gauthier, Y. Luo, F. Paul, B. Fabre, F. Barrière, S. Ababou-Girard, T. Roisnel and M. G. Humphrey, *J. Phys. Chem. C*, 2014, **118**, 3680.
20 L. S. Mpeta, G. Fomo and T. Nyokong, *J. Coord. Chem.*, 2018, **71**, 1623.
21 G. J. Leigh and C. J. Pickett, *J. Chem. Soc., Dalton Trans.*, 1977, 1797.
22 D. L. DuBois, *Inorg. Chem.*, 1984, **23**, 2047.
23 T. A. George and B. B. Kaul, *Inorg. Chem.*, 1990, **29**, 4969.
24 D. V. Yandulov and R. R. Schrock, *Science*, 2003, **301**, 76.
25 J. S. Anderson, J. Rittle and J. C. Peters, *Nature*, 2013, **501**, 84.
26 S. E. Creutz and J. C. Peters, *J. Am. Chem. Soc.*, 2014, **136**, 1105.
27 T. A. Engesser, A. Kindjajev, J. Junge, J. Krahmer and F. Tuczek, *Chemistry*, 2020, **26**, 14807.
28 A.-M. Vogt, T. A. Engesser, J. Krahmer, N. Michaelis, M. Pfeil, J. Junge, C. Näther, N. Le Poul and F. Tuczek, *Angew. Chem., Int. Ed.*, 2025, **64**, e202420220.
29 S. J. K. Forrest, B. Schluschaß, E. Y. Yuzik-Klimova and S. Schneider, *Chem. Rev.*, 2021, **121**, 6522.
30 Y. Ashida, T. Mizushima, K. Arashiba, A. Egi, H. Tanaka, K. Yoshizawa and Y. Nishibayashi, *Nat. Synth.*, 2023, **2**, 635.

31 Q. J. Bruch, S. Malakar, A. S. Goldman and A. J. M. Miller, *Inorg. Chem.*, 2022, **61**, 2307.
32 I. Klopsch, M. Finger, C. Würtele, B. Milde, D. B. Werz and S. Schneider, *J. Am. Chem. Soc.*, 2014, **136**, 6881.
33 Y. Ashida, K. Arashiba, K. Nakajima and Y. Nishibayashi, *Nature*, 2019, **568**, 536.
34 K. Arashiba, E. Kinoshita, S. Kuriyama, A. Eizawa, K. Nakajima, H. Tanaka, K. Yoshizawa and Y. Nishibayashi, *J. Am. Chem. Soc.*, 2015, **137**, 5666.
35 Q. Liao, N. Saffon-Merceron and N. Mézailles, *ACS Catal.*, 2015, **5**, 6902.
36 B. Schluschaß, J. Abbenseth, S. Demeshko, M. Finger, A. Franke, C. Herwig, C. Würtele, I. Ivanovic-Burmazovic, C. Limberg, J. Telser, *et al.*, *Chem. Sci.*, 2019, **10**, 10275.
37 B. M. Lindley, R. S. van Alten, M. Finger, F. Schendzielorz, C. Würtele, A. J. M. Miller, I. Siewert and S. Schneider, *J. Am. Chem. Soc.*, 2018, **140**, 7922.
38 S. Mandal, X. Zhou, Q. J. Bruch, R. N. Allen, L. W. Giordano, N. J. I. Walker, T. J. Emge, F. Hasanayn, A. J. M. Miller, S. Malakar, *et al.*, *Chem. Sci.*, 2025, **16**, 7347.
39 L. Eberle and J. Ballmann, *J. Am. Chem. Soc.*, 2024, **146**, 7979.
40 P. Garrido-Barros, J. Derosa, M. J. Chalkley and J. C. Peters, *Nature*, 2022, **609**, 71.
41 A. F. Ibrahim, P. Garrido-Barros and J. C. Peters, *ACS Catal.*, 2023, **13**, 72.
42 L. Merakeb, S. Bennaamane, J. de Freitas, E. Clot, N. Mézailles and M. Robert, *Angew. Chem., Int. Ed.*, 2022, **61**, e202209899.
43 K. U. Clausen, A. Schlimm, K. Bedbur, C. Näther, T. Strunskus, L. Fu, M. Gruber, R. Berndt and F. Tuczek, *Chem. – Eur. J.*, 2024, **30**, e202303912.
44 K. U. Clausen, N. Pienack, J. Gripp and F. Tuczek, *Chem. – Eur. J.*, 2024, **30**, e202304359.
45 A. Schlimm, N. Stucke, B. M. Flöser, T. Rusch, J. Krahmer, C. Näther, T. Strunskus, O. M. Magnussen and F. Tuczek, *Chem. – Eur. J.*, 2018, **24**, 10732.
46 F. Petersen, I. Lautenschläger, A. Schlimm, B. M. Flöser, H. Jacob, R. Amirbeigiarab, T. R. Rusch, T. Strunskus, O. Magnussen and F. Tuczek, *J. Chem. Soc., Dalton Trans.*, 2021, 1042.
47 G. C. Stephan, C. Sivasankar, F. Studt and F. Tuczek, *Chemistry*, 2008, **14**, 644.
48 N. Hazari, *Chem. Soc. Rev.*, 2010, **39**, 4044.
49 K. G. Caulton, R. L. DeKock and R. F. Fenske, *J. Am. Chem. Soc.*, 1970, **92**, 515.
50 M. Fritz, S. Demeshko, C. Würtele, M. Finger and S. Schneider, *Eur. J. Inorg. Chem.*, 2023, 26.
51 H. Jacob, S. Ulrich, U. Jung, S. Lemke, T. Rusch, C. Schütt, F. Petersen, T. Strunskus, O. Magnussen, R. Herges, *et al.*, *Phys. Chem. Chem. Phys.*, 2014, **16**, 22643.
52 W. Hewertson and H. R. Watson, *J. Chem. Soc.*, 1962, 1490.
53 A. M. Bond, R. Colton, S. W. Feldberg, P. J. Mahon and T. Whyte, *Organometallics*, 1991, **10**, 3320.
54 R. G. Compton, J. C. Eklund, A. Hallik, S. Kumbhat, A. M. Bond and R. Colton, *J. Chem. Soc., Perkin Trans. 2*, 1995, 1327.
55 M. C. Favas, D. L. Kepert, B. W. Skelton and A. H. White, *J. Chem. Soc., Dalton Trans.*, 1980, 447.
56 J. Chatt and H. R. Watson, *J. Chem. Soc.*, 1961, 4980.
57 D. L. Miller, B. J. Boro, K. Grubel, M. L. Helm and A. M. Appel, *Eur. J. Inorg. Chem.*, 2015, **2015**, 5781.
58 N. T. Lucas, M. P. Cifuentes, L. T. Nguyen and M. G. Humphrey, *J. Cluster Sci.*, 2001, **12**, 201.
59 S. Zhang, Z. Zhang and R. Cao, *Inorg. Chim. Acta*, 2017, **461**, 57.
60 R. B. King and P. N. Kapoor, *J. Am. Chem. Soc.*, 1971, **93**, 4158.
61 D. L. DuBois, W. H. Myers and D. W. Meek, *J. Chem. Soc., Dalton Trans.*, 1975, 1011.
62 W. Strohmeier and F.-J. Müller, *Chem. Ber.*, 1967, **100**, 2812.
63 C. Christiansen, *Ann. Phys.*, 1884, **259**, 298.
64 C. Christiansen, *Ann. Phys.*, 1885, **260**, 439.
65 C. V. Raman, *PINSA-A:Proc. Indian Natl. Sci. Acad., Part A*, 1949, **29**, 381.
66 J. Talarmin, T. I. Al-Salih, C. J. Pickett, G. E. Bossard, T. A. George and C. M. Duff-Spence, *J. Chem. Soc., Dalton Trans.*, 1992, 2263.
67 J. C. Love, L. A. Estroff, J. K. Kriebel, R. G. Nuzzo and G. M. Whitesides, *Chem. Rev.*, 2005, **105**, 1103.
68 H. S. Hansen, S. Tougaard and H. Biebuyck, *J. Electron Spectrosc. Relat. Phenom.*, 1992, **58**, 141.
69 G. E. Poirier and M. J. Tarlov, *Langmuir*, 1994, **10**, 2853.
70 M. D. Porter, T. B. Bright, D. L. Allara and C. E. D. Chidsey, *J. Am. Chem. Soc.*, 1987, **109**, 3559.
71 S. Bian, K. B. Schesing and A. B. Braunschweig, *Chem. Commun.*, 2012, **48**, 4995.
72 M. G. Williams and A. V. Teplyakov, *Appl. Surf. Sci.*, 2016, **388**, 461.
73 J. P. Collman, N. K. Devaraj, T. P. A. Eberspacher and C. E. D. Chidsey, *Langmuir*, 2006, **22**, 2457.
74 A. Saad, M. Abderrabba and M. M. Chehimi, *Surf. Interface Anal.*, 2016, **49**, 340.
75 T. Heinrich, C. H.-H. Traulsen, E. Darlatt, R. Sebastian, J. Poppenberg, N. L. Traulsen, I. Linder, A. Lippitz, P. M. Dietrich, B. Dib, *et al.*, *RSC Adv.*, 2014, **4**, 17694.
76 T. M. Willey, A. L. Vance, T. van Buuren, C. Bostedt, L. J. Terminello and C. S. Fadley, *Surf. Sci.*, 2005, **576**, 188.
77 Y. Ge, T. Weidner, H. Ahn, J. E. Whitten and M. Zharnikov, *J. Phys. Chem. C*, 2009, **113**, 4575.
78 M. I. Béthencourt, L. Srisombat, P. Chinwangso and T. R. Lee, *Langmuir*, 2009, **25**, 1265.
79 D. G. Castner, K. Hinds and D. W. Grainger, *Langmuir*, 1996, **12**, 5083.
80 H. B. Lu, C. T. Campbell and D. G. Castner, *Langmuir*, 2000, **16**, 1711.
81 N. Nishida, M. Hara, H. Sasabe and W. Knoll, *Jpn. J. Appl. Phys.*, 1996, **35**, L799.

82 A. Mulas, Y.-M. Hervault, X. He, E. Di Piazza, L. Norel, S. Rigaut and C. Lagrost, *Langmuir*, 2015, **31**, 7138.
83 T. Ishida, M. Hara, I. Kojima, S. Tsuneda, N. Nishida, H. Sasabe and W. Knoll, *Langmuir*, 1998, **14**, 2092.
84 H. Jacob, K. Kathirvel, F. Petersen, T. Strunskus, A. Bannwarth, S. Meyer and F. Tuczek, *Langmuir*, 2013, **29**, 8534.
85 A. Shaporenko, A. Terfort, M. Grunze and M. Zharnikov, *J. Electron Spectrosc. Relat. Phenom.*, 2006, **151**, 45.
86 C.-J. Zhong, R. C. Brush, J. Anderegg and M. D. Porter, *Langmuir*, 1999, **15**, 518.
87 Y. W. Yang and L. J. Fan, *Langmuir*, 2002, **18**, 1157.
88 J. Huang and J. C. Hemminger, *J. Am. Chem. Soc.*, 1993, **115**, 3342.
89 M. Lewis, M. Tarlov and K. Carron, *J. Am. Chem. Soc.*, 1995, **117**, 9574.
90 Y. Zhang, R. H. Terrill and P. W. Bohn, *Chem. Mater.*, 1999, **11**, 2191.
91 E. Ito, H. Kang, D. Lee, J. B. Park, M. Hara and J. Noh, *J. Colloid Interface Sci.*, 2013, **394**, 522.
92 G. Feng, T. Niu, X. You, Z. Wan, Q. Kong and S. Bi, *Analyst*, 2011, **136**, 5058.
93 M. E. Vela, H. Martin, C. Vericat, G. Andreasen, A. Hernández Creus and R. C. Salvarezza, *J. Phys. Chem. B*, 2000, **104**, 11878.
94 J. Dai, Z. Li, J. Jin, Y. Shi, J. Cheng, J. Kong and S. Bi, *Biosens. Bioelectron.*, 2009, **24**, 1074.
95 M. M. Walczak, D. D. Popenoe, R. S. Deinhammer, B. D. Lamp, C. Chung and M. D. Porter, *Langmuir*, 1991, **7**, 2687.
96 L. Jiang, L. Yuan, L. Cao and C. A. Nijhuis, *J. Am. Chem. Soc.*, 2014, **136**, 1982.
97 N. T. Flynn, T. N. T. Tran, M. J. Cima and R. Langer, *Langmuir*, 2003, **19**, 10909.
98 C. E. Chidsey and R. W. Murray, *Science*, 1986, **231**, 25.
99 D. M. Adams, L. Brus, C. E. D. Chidsey, S. Creager, C. Creutz, C. R. Kagan, P. V. Kamat, M. Lieberman, S. Lindsay, R. A. Marcus, *et al.*, *J. Phys. Chem. B*, 2003, **107**, 6668.
100 G. Benítez, C. Vericat, S. Tanco, F. Remes Lenicov, M. F. Castez, M. E. Vela and R. C. Salvarezza, *Langmuir*, 2004, **20**, 5030.
101 C. Vericat, F. R. Lenicov, S. Tanco, G. Andreasen, M. E. Vela and R. C. Salvarezza, *J. Phys. Chem. B*, 2002, **106**, 9114.
102 J. P. Collman, N. K. Devaraj and C. E. D. Chidsey, *Langmuir*, 2004, **20**, 1051.
103 A. Gomila, N. Le Poul, N. Cosquer, J.-M. Kerbaol, J.-M. Noël, M. T. Reddy, I. Jabin, O. Reinaud, F. Conan and Y. Le Mest, *J. Chem. Soc., Dalton Trans.*, 2010, 11516.
104 P. Krysiński, M. Brzostowska-Smolska and M. Mazur, *Mater. Sci. Eng., C*, 1999, **8–9**, 551.
105 N. C. Ramos, J. W. Medlin and A. Holewinski, *ACS. Appl. Mater Interfaces*, 2023, **15**, 14470–14480.
106 L. Wang, Q. Ran, Y. Tian, J. Xu, Y. Xian, R. Peng and L. Jin, *J. Colloid Interface Sci.*, 2010, **350**, 544.
107 S. R. Nxele, P. Mashazi and T. Nyokong, *Electroanalysis*, 2015, **27**, 2468.
108 O. Karagollu, M. Gorur, F. Gode, B. Sennik and F. Yilmaz, *Sens. Actuators, B*, 2014, **193**, 788.
109 A. Koch, T. A. Engesser, C. Näther and F. Tuczek, *ChemCatChem*, 2024, **16**, e202301316.
110 D. Brunel, V. Jangid, E. Sanchez Adaime, D. Duché, A. K. Bharwal, M. Abel, M. Koudia, T. Buffeteau, C. Lebouin, J. J. Simon, *et al.*, *Appl. Surf. Sci.*, 2021, **566**, 150731.
111 L. Wang, U. S. Schubert and S. Hoeppener, *Chem. Soc. Rev.*, 2021, **50**, 6507.
112 R. G. Greenler, *J. Chem. Phys.*, 1966, **44**, 310.
113 R. Arnold, A. Terfort and C. Wöll, *Langmuir*, 2001, **17**, 4980.
114 A. Früh, S. Rutkowski, I. O. Akimchenko, S. I. Tverdokhlebov and J. Frueh, *Appl. Surf. Sci.*, 2022, **594**, 153476.
115 D. L. Allara, A. Baca and C. A. Pryde, *Macromolecules*, 1978, **11**, 1215.
116 D. L. Allara and R. G. Nuzzo, *Langmuir*, 1985, **1**, 52.
117 D. L. Allara and R. G. Nuzzo, *Langmuir*, 1985, **1**, 45.
118 M. K. Debe, *J. Appl. Phys.*, 1984, **55**, 3354.
119 C. J. Miller, F. M. Brunner, H. R. Kelly, P. L. Cheung, N. A. Torquato, M. Gembicky, S. Okuno, T. Chan, V. S. Batista and C. P. Kubiak, *J. Chem. Soc., Dalton Trans.*, 2022, 17688.
120 L. Sang, A. Mudalige, A. K. Sigdel, A. J. Giordano, S. R. Marder, J. J. Berry and J. E. Pemberton, *Langmuir*, 2015, **31**, 5603.
121 I. Zawisza, X. Bin and J. Lipkowski, *Langmuir*, 2007, **23**, 5180.
122 M. Gliboff, L. Sang, K. M. Knesting, M. C. Schalnat, A. Mudalige, E. L. Ratcliff, H. Li, A. K. Sigdel, A. J. Giordano, J. J. Berry, *et al.*, *Langmuir*, 2013, **29**, 2166.
123 J. M. Palasz, Z. Long, J. Meng, P. E. Videla, H. R. Kelly, T. Lian, V. S. Batista and C. P. Kubiak, *J. Am. Chem. Soc.*, 2024, **146**, 10489.
124 S. Grimme, C. Bannwarth and P. Shushkov, *J. Chem. Theory Comput.*, 2017, **13**, 1989.
125 C. Bannwarth, E. Caldeweyher, S. Ehlert, A. Hansen, P. Pracht, J. Seibert, S. Spicher and S. Grimme, *WIREs Comput. Mol. Sci.*, 2021, **11**, e1493.
126 A. Mattiuzzi, I. Jabin, C. Mangeney, C. Roux, O. Reinaud, L. Santos, J.-F. Bergamini, P. Hapiot and C. Lagrost, *Nat. Commun.*, 2012, **3**, 1130.
127 B. Martinez, Y. R. Leroux, P. Hapiot and C. S. Henry, *ACS. Appl. Mater Interfaces*, 2023, **15**, 50780–50788.
128 M. Taras, J.-F. Bergamini, P. A. Brooksby, P. Hapiot, C. Lagrost and Y. R. Leroux, *RSC Appl. Interfaces*, 2024, **1**, 734.
129 Y. Aceta, Y. R. Leroux and P. Hapiot, *ChemElectroChem*, 2019, **6**, 1704.
130 *Handbuch der Präparativen Anorganischen Chemie. in drei Bänden*, ed. G. Brauer, Ferdinand Enke Verlag, Stuttgart, 1981.

131 R. B. King, *J. Organomet. Chem.*, 1967, **8**, 139.
132 D. M. Nguyen, A. Frazer, L. Rodriguez and K. D. Belfield, *Chem. Mater.*, 2010, **22**, 3472.
133 G. M. Sheldrick, *Acta Crystallogr., Sect. A: Found. Adv.*, 2015, **71**, 3.
134 G. M. Sheldrick, *Acta Crystallogr., Sect. C: Struct. Chem.*, 2015, **71**, 3.
135 J. C. Hoogvliet, M. Dijksma, B. Kamp and W. P. van Bennekom, *Anal. Chem.*, 2000, **72**, 2016.
136 A. Sarapuu, K. Tammeveski, T. T. Tenno, V. Sammelselg, K. Kontturi and D. J. Schiffrin, *Electrochem. Commun.*, 2001, **3**, 446.
137 F. Neese, *Wiley Interdiscip. Rev.: Comput. Mol. Sci.*, 2022, **12**, e1606.
138 F. Neese, *J. Comput. Chem.*, 2023, **44**, 381–396.
139 F. Neese, *J. Comput. Chem.*, 2003, **24**, 1740.
140 F. Weigend and R. Ahlrichs, *Phys. Chem. Chem. Phys.*, 2005, **7**, 3297.